Mémoire

Auteur : Sogan, Michel
Promoteur(s) : 28925; Far, Johann
Faculté : Faculté des Sciences
Diplôme : Master en sciences spatiales, à finalité approfondie
Année académique : 2024-2025
URI/URL : http://hdl.handle.net/2268.2/23897

Master's Degree in Space Sciences, Research Focus
Faculty of Sciences at the University of Liège

Master's Thesis in the Unit for Space Research and Planetary Sciences at the University of Bern

OpenTOF, a Compact and Novel Mass Spectrometer for Fast Spacecraft Flybys: Molecular Measurements Free of Fragmentation at Hypervelocity Encounters.

Michael Sogan

Academic Year 2024 – 2025

Submitted on 18 August 2025

Assessment Committee

Dr. Rico Fausch in Bern, member of the committee
Prof. Dr. Peter Wurz in Bern, co-supervisor
Dr. Johann Far in Liège, co-supervisor
Prof. Dr. Denis Grodent in Liège, member of the committee
Prof. Dr. Benoît Hubert in Liège, member of the committee

Abstract

The exploration of the Solar System is important to understand the origin and evolution of celestial bodies in a planetary system and to gather information about the possible appearance and development of life on other bodies than the Earth. In this endeavour, the study of the upper layers of the Earth's atmosphere, the characterisation of the plumes on Enceladus and Europa, or the investigation of Io all contribute to discovering a more global and complete picture. In this context, with the aim to gather needed data since in situ measurements are needed, the Unit for Space Research and Planetary Sciences in Bern developed a compact mass spectrometer for space applications, featuring a novel gas inlet labelled Direct Open Source (DOeS). This new instrument is designed to measure ions and neutral molecules at high relative speeds up to 20 km/s, thus enabling fast spacecraft flybys of the targeted atmospheres, without high relative velocity impact fragmentation to preserve parent molecules. Building up on previous contributions to the project, this work prepared a compact setup with an ion and neutral beam, called LEIS, to test mass spectrometers. Furthermore, OpenTOF was tested and optimised voltage sets of the instrument were found for several speeds, especially 10 km/s and 20 km/s. For fast ions, masses up to m/z 293 were measured above 11 km/s, while masses m/z below 69 were detected at speeds above 23 km/s. Finally, first tests with fast molecules were already successful. Masses up to m/z 136 were detected at 17 km/s. This work delivered a proof of concept, showing that the instrument and its novel gas inlet fulfil their purposes at high relative velocities. Therefore, OpenTOF was proven to be a promising instrument for the near-future investigation of atmospheres in the Solar System.

Contents

Chapter 1

Introduction

1.1 Scientific Context

The Sun is surrounded by only eight planets. So far, life has only been detected on Earth. However, numerous different celestial bodies populate the Solar System: dwarf planets such as Pluto, asteroids, comets, or natural satellites such as the Moon. Even though the Moon might be the most famous natural satellite to the public since it illuminates clear night skies on Earth, it is not at all alone in the Solar System. As of early 2025, Jupiter, a gas giant and the fifth planet with regards to distance to the Sun, possess over 95 known natural satellites. Moreover, Saturn, the sixth planet and also a gas giant, has 146 registered moons as of early 2025. New natural satellites are still discovered every year (Sheppard et al., 2023). This shows that many mysteries of the Solar System have yet still to be unravelled and that a keen interest exists within the scientific community. The study of these natural satellites is useful to understand the origin and evolution of celestial bodies in a planetary system and to gather information about the possible appearance and development of life on other bodies than the Earth. Thus, Jupiter's moon Io is relevant to the study of the Solar System's evolution due to its strongly active volcanism. Furthermore, Enceladus, one other moon of Jupiter, and Europa, one of Saturn's moons, both have subsurface oceans and plumes of vapour which spout out of the surface, hence the link to hidden chemical biosignatures. However, sensitivity and spatial resolution are limited when measurements are carried out by remote-sensing techniques on Earth or in the vicinity of it. Therefore, in situ measurements by mass spectrometers are needed in missions during which the relative velocity between the spacecraft and the target can reach 20 km/s (Fausch et al. (2022b) and references therein).

1.1.1 Knowledge about the Targeted Moons

Enceladus

The Cassini-Huygens spacecraft was launched in 1997 and investigated the Saturnian system (Flamini et al., 2019). Fulfilling many accomplishments, it also revealed the subsurface ocean of Saturn's moon Enceladus (Flamini et al., 2019; MacKenzie et al., 2022).

Enceladus has a width of about 500 km and a long-lasting plume spouting out of the South Polar Terrain (SPT). The fact that there are fewer craters on the SPT than in other regions shows a recent geological activity. Furthermore, observations and modelling of the plume indicate that this activity could be long-lived (MacKenzie et al. (2022) and references therein).

Material discovered in the plume hints towards a geochemical interaction between the subsurface ocean and a rocky core that could unbalance the chemical equilibrium. As a comparison, seafloors on

Earth have hydrothermal systems releasing CO_2, CH_4, and H_2. Thus, these chemicals can be used as a source of chemical energy by the most primitive forms of life (MacKenzie et al., 2022; Reveillaud et al., 2016). Moreover, living organisms have been found in extreme ecosystems on Earth, such as in light-independent environment in the crust, at the bottom of the ocean, or even below layers of ice with a thickness of several kilometers (MacKenzie et al. (2022) and references therein). Thus, this moon of Saturn mainly displays remarkable characteristics because of its subsurface ocean, energy sources, and potentially available chemical blocks (MacKenzie et al. (2022) and references therein). Therefore, an interest has been growing in the past years to target Enceladus with in situ measurements to further investigate its potential for sheltering life.

Io

Io, a Galilean satellite with a mean diameter of $3,643\ km$, orbits closest to Jupiter. Thus, Io's eccentric orbit causes gravitational variations, which lead to tidal deformations. These deformations on Io are expected to contribute to the strong volcanism as the main source of energy (Park et al. (2024) and references therein). As a consequence, the highly intense volcanic activities seem to corroborate the claim that Io's interior is at least partially molten. Moreover, gravitational measurements support the existence of a metallic core, probably in a liquid state (Park et al. (2024) and references therein).

Melt is thought to be quickly transported from partially molten areas in the interior and could either directly be spouted out through the crust, or could firstly gather into a magma ocean below the crust before eruptions (Park et al. (2024) and references therein). However, a shallow global magma ocean on Io would lead to a strong tidal deformation, while a mostly solid mantle would mean a more rigid structure and, therefore, a weaker change in shape. Consequently, recent measurements of Io's tidal deformations carried out by Park et al. (2024) tend to show that the moon has a partially molten but mostly solid interior without a global magma ocean.

The Upper Layers of the Earth's Atmosphere

The study of the upper layers of Earth's atmosphere can, among several scientific benefits, help to understand atmospheric processes, the long-term evolution of the atmosphere and differences with other planets, or create more accurate models. However, the available data is outdated. Therefore, new measurements of both the chemical composition and the density of the exosphere are simultaneously needed (Fausch et al. (2020, 2022) and references therein). OpenTOF could be mounted on a small satellite or flown on board the International Space Station (ISS), which fly on a Low-Earth Orbit (LEO). A typical speed for a spacecraft in LEO is 7.65 km/s (Chan and Zhou, 2018).

1.2 Outline of this Work

CubesatTOF is a miniaturised mass spectrometer built at the Unit for Space Research and Planetary Sciences in the Faculty of Sciences at the University of Bern. It was specially designed to target the upper layers of Earth's atmosphere on board a cubesat (Fausch et al., 2022). OpenTOF, also in development by the same team, is a slightly larger mass spectrometer with a typical dimension of about 25 cm. OpenTOF's design was inspired by CubeSatTOF, so both belong to the same family of instruments. Thus, measurements and tests on OpenTOF might also be relevant to the development of CubeSatTOF. However, while staying a compact device, OpenTOF aims for a wider mass range than CubeSatTOF with m/z 1 to 800 for speeds up to 20 km/s or even m/z 1000 for lower velocities (Fausch et al., 2022a; Schertenleib, 2023). Therefore, OpenTOF's design is suitable

for missions seeking to investigate scientific subjects as explained in Section 1.1. Furthermore, this family of instruments use a novel gas inlet to enable direct measurements without fragmentation due to high-velocity impact, as detailed in Section 1.5.

The adaptation from CubeSatTOF to OpenTOF was designed by Schertenleib (2023) and the first setup to test the instrument in thermal mode was built by Iseli (2024). Consequently, this work is a continuation of their tasks. The objectives of this work were to prepare a setup to test mass spectrometers with ions at velocities up to 20 km/s, upgrade the setup to enable tests on mass spectrometers with fast gas at velocities up to 20 km/s, test the setup on OpenTOF, and find preliminary optimised voltage sets for OpenTOF at 10 km/s and at 20 km/s.

Chapter 1 gives background information on the instrument. Chapter 2 explains the tests to prepare LEIS, the device generating the ion beam and the fast neutral beam. Then, Chapter 3 shows the first results with fast ions. Furthermore, Chapter 4 discusses the detection of fast neutrals without fragmentation thanks to the novel gas inlet. Finally, Chapter 5 concludes about the achievements and hints towards solutions for future improvement of the testing setup.

1.3 Brief Introduction to Mass Spectrometry

The main principle of mass spectrometry is to use accelerations or velocities that depend on the specific mass of the studied substance to compute the mass and, therefore, to determine what exact molecules compose a given sample. Spaceborne mass spectrometers are highly useful for in situ measurement to get accurate data about the composition and abundances in the investigated atmosphere of the celestial body.

In 1912, J. J. Thomson built his parabola spectrograph: the first mass spectrometer. W. Stephens proposed the concept of a linear time-of-flight mass spectrometer in 1946. A. E. Cameron and D. F. Eggers published their design and the obtained mass spectra for such a mass spectrometer in 1948 (de Hoffmann and Stroobant, 2007).

Nowadays, mass spectrometers are compact enough to be mounted on medium- to large-sized satellites or even miniaturised and sent to space on a cubesat. Several kinds of devices exist based on different sorts of mass analysers, such as time-of-flight, quadrupole, ion trap, electrostatic trap, magnetic and electromagnetic sections, or ion cyclotron resonance (de Hoffmann and Stroobant, 2007). This work focuses on the OpenTOF instrument, which relies on the principles of time-of-flight mass spectrometry (ToF-MS) described in Section 1.3.1.

1.3.1 Time-of-Flight Mass Spectrometry ToF-MS

A mass spectrometer needs high vacuum conditions to properly work, because the studied ions need to travel with little interference with present gas molecules. Otherwise, collisions between ions and gas molecules can take the ions off their path to end up on the walls of the device instead of on its detector. Moreover, these collisions might also lead to undesired reactions that could change the sample and result in more complex spectra. Finally, instruments using high voltages also need a pressure low enough to prevent electrical discharges (de Hoffmann and Stroobant (2007)).

Figure 1.1 shows the schematic of a simplified time-of-flight mass spectrometer. The subsequent steps occur from left to right on the drawing. Firstly, if it is not already in gaseous phase, the sample to be studied is vaporised and, then, let in from the left side. Secondly, the gas is brought to a zone in which it is ionised. Thirdly, the positive ions are accelerated between x_a and x_b by an electric field, before entering the mass analyser. That last long section of the mass spectrometer consists of a

field-free drift tube in which less massive ions are faster than more massive ions travelling alongside them. Finally, all particles fall onto the detector and their specific times of flight may be recorded.

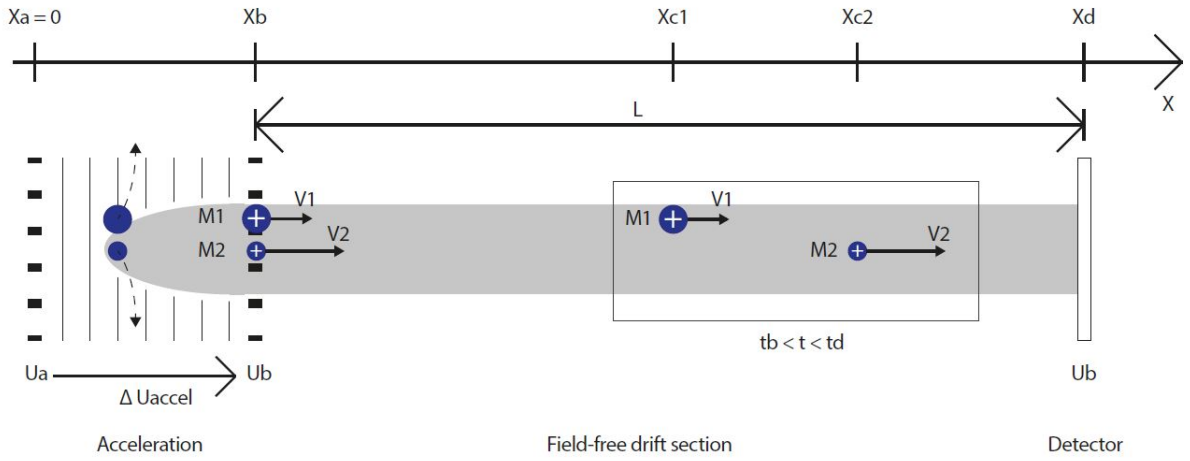

Figure 1.1: Situation 1. A simplified schematic of a time-of-flight mass spectrometer to illustrate its main working principles.

The working principles of a time-of-flight mass spectrometer might be illustrated thanks to a thought experiment considering two particles. Let m_1 and m_2 be the masses and let v_1 and v_2 be the speeds of particle 1 and particle 2, respectively. If particle 1 is an argon Ar atom (39.962 u for isotope 40) and particle 2 is a krypton Kr atom (83.911 u for isotope 84), then $m_1 = 6.636 \cdot 10^{-26}\ kg$ and $m_2 = 1.393\ \cdot\ 10^{-25}\ kg$ according to the CODATA 2022 recommended values (Tiesinga et al., 2022). The mass difference between the atoms and their corresponding ions is negligible in a first approach. After being ionised one time on the left of the grid positioned at x_b, both ions Ar^+ and Kr^+ are accelerated up to the other grid at x_b. The electric potential at x_a is called U_a and the electric potential at x_b is labelled U_b. Thus, the acceleration voltage ΔU_{Accel} for both ions has a value of U_b - U_a. For the sake of this simplified example, it is assumed that both ions reach that exact same position x_b on the exact same time $t = t_b$. Since no difference of electric potential is applied to the ions on the right of x_b, they will keep their velocities constant in the final section of the mass spectrometer. The velocities are assumed to be perpendicular to the acceleration grids and, thus, parallel to the drift tube. Therefore, knowing the speeds at position x_b, one may compute the times t_d^{Ar} and t_d^{Kr} needed for each ion to travel through the drift tube and reach the detector at position x_d.

Both ions are positively charged, so applying a positive potential on x_a and a lower value on x_b once the ions have entered this zone will push them towards the right. ΔU_{Accel} is assumed to be 600 V. Thus, the kinetic energies of both ions E_{kin}^{Ar} and E_{kin}^{Kr} at position x_b are the same, since the initial thermal energy might be neglected and both ions carry the same electric charge $e\ =\ 1.602176634 \cdot\ 10^{-19}\ C$. The energy is provided by the electric tension:

$$E_{kin}^{Ar} = E_{kin}^{Kr} = \Delta U_{Accel} \cdot e = 9.613 \cdot\ 10^{-17} J.$$

Both ions carry the same kinetic energy. However, having different masses, they travel with a different speed, as is shown in the expression for the kinetic energy:

$$E_{kin}^{Ar} = \frac{1}{2} \cdot m_1 \cdot v_1^2. \tag{1.1}$$

The equation (1.1) of the kinetic energy for argon yields

$$v_1 = \sqrt{\frac{2 \cdot E_{kin}^{Ar}}{m_1}} = 53,836.1 \ m/s.$$

For krypton the speed is

$$v_2 = \sqrt{\frac{2 \cdot E_{kin}^{Kr}}{m_2}} = 37,145.9 \ m/s.$$

The length of the drift tube $L = x_d - x_b$ is assumed to be 0.21 m. Furthermore, the time needed for the ion to travel from x_b to x_d is labelled Δt_d^{Ar} for argon and Δt_d^{Kr} for krypton and can be determined thanks to the speeds and the flight length:

$$\Delta t_d^{Ar} = \frac{L}{v_1} = \frac{0.21}{53,836.1} = 3.90 \ \cdot \ 10^{-6} s.$$

$$\Delta t_d^{Kr} = \frac{L}{v_2} = \frac{0.21}{37,145.9} = 5.65 \ \cdot \ 10^{-6} s.$$

As expected, argon, which is less massive than krypton, arrives at the detector before krypton. The detections might be recorded in a plot showing the number of ions arriving at the detector as a function of time with $t = t_b$ as the starting time, as is illustrated in Figure 1.2.

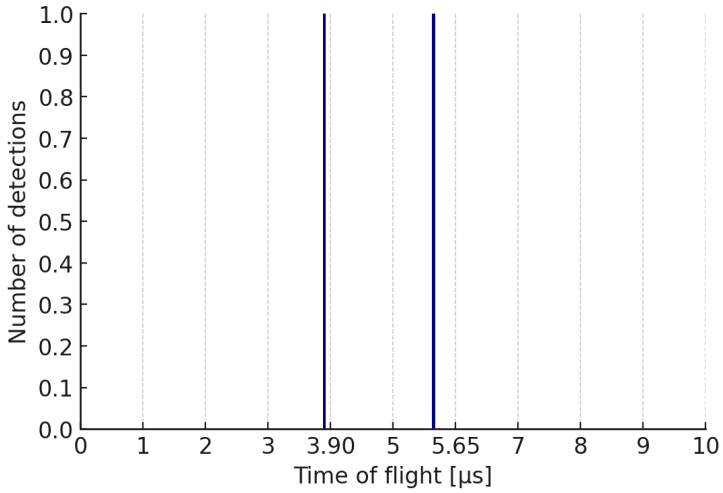

Figure 1.2: Detected ions of simplified situation 1, recorded in a so-called mass spectrum. The ordinate is the number of ions and the abscissa represents the measured time of flight.

Instead of the time of flight on the abscissa, the masses might be displayed, as on Figure 1.3. This bar plot shows the less massive ion, argon, on the left at a lower flight time and the more massive ion, krypton, on the right at a higher flight time. As a consequence, these two detections define three zones on the plot: masses lower than argon on the left, masses higher than krypton on the

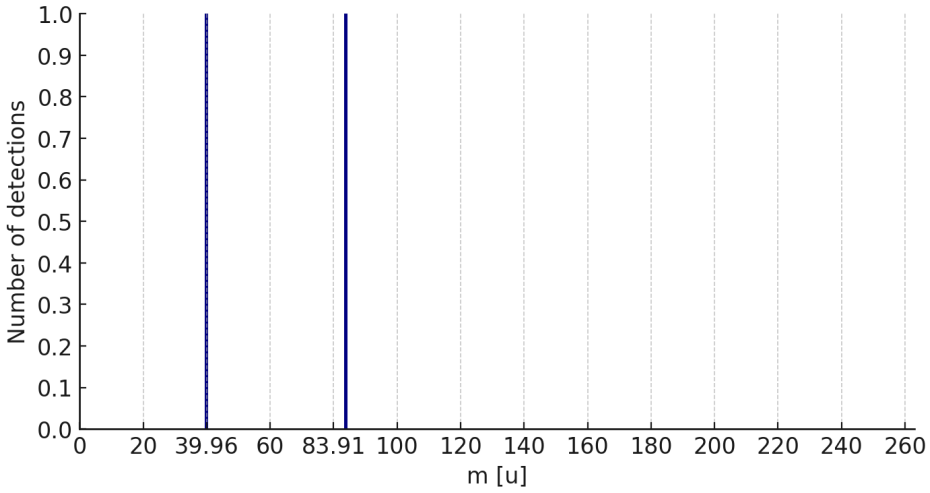

Figure 1.3: Calibrated mass spectrum of situation 1. Contrary to Figure 1.2 the abscissa is calibrated to represent the mass.

right, and masses in between those two values in the centre. As seen with the numerical application of situation 1, a lighter particle will have a shorter time of flight, so will be displayed on the left of the plot, while a heavier particle, with a longer time of flight, will appear on the right of the graphic. Therefore, if another particle with an unknown mass is detected by the mass spectrometer, its time of flight can reveal information about its mass thanks to a comparison with argon or krypton.

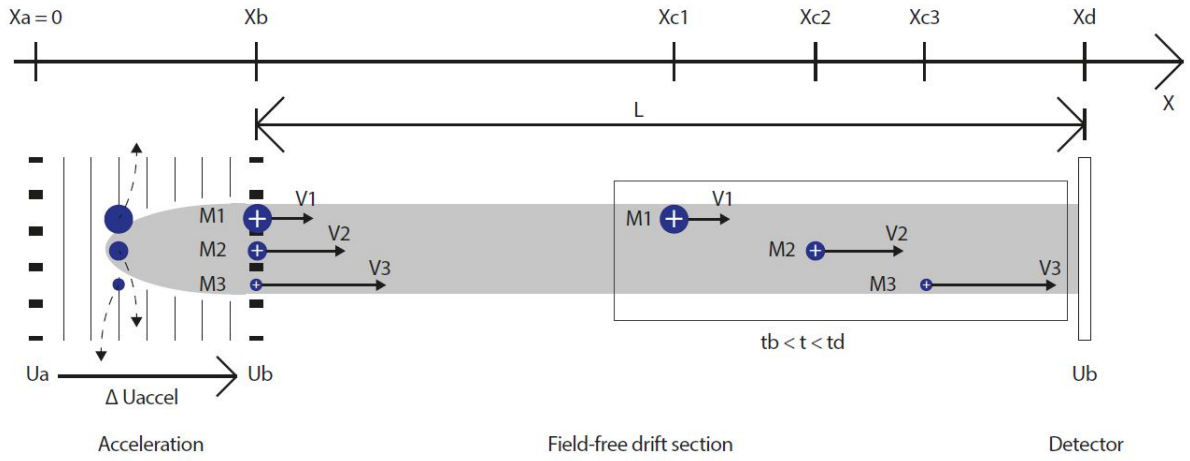

Figure 1.4: Situation 2. A simplified schematic of a time-of-flight mass spectrometer to illustrate its main working principles with three particles.

Based on this first example, a second similar situation with a third particle may be studied. The variables for particle 1 and 2 and their values stay unchanged, while m_3 and v_3 represent the mass and the speed of particle 3. Figure 1.4 shows situation 2. The argon atom (with mass m_1), the krypton atom (with mass m_2), and the third particle (with mass m_3) are all ionised on the left of the system and, then, accelerated by the same electric field to reach x_b. Again as a simplification, it is assumed that all three particles start their journey on position x_b, exactly at the same time $t = t_b$, with velocities perpendicular to the grids and parallel to the drift tube. Finally, they all fall onto

the detector and their times of flight are recorded. The measurements of this thought experiment are displayed in Figure 1.5.

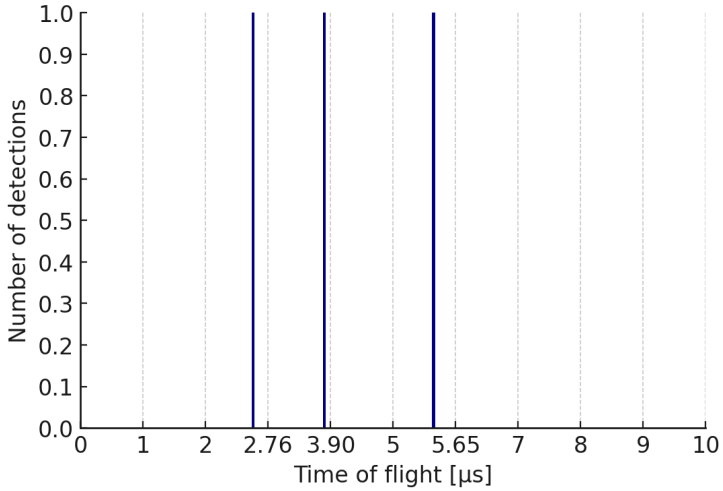

Figure 1.5: Uncalibrated mass spectrum of situation 2. The number of particles detected is displayed as a function of the time of flight.

Figure 1.5 shows the same times of flight for argon and for krypton as in Figure 1.2. Furthermore, the third particle has a shorter time of flight $\Delta t_3 = 2.759$ μs. Therefore, particle 3 seems to have a lower mass than argon. Furthermore, its speed may be determined from the length of the drift tube L:

$$v_3 = \frac{L}{\Delta t_3} = 76,122.1 \ m/s.$$

Assuming that the particle is only ionised once (so the energy is $U \cdot e$), it is possible to compute the corresponding mass rewriting Equation 1.1 for m_3 ($v_3 > 0$):

$$E_{kin}^{P_3} = \frac{1}{2} \cdot m_3 \cdot v_3^2 \Leftrightarrow \tag{1.2}$$

$$m_3 = \frac{2 \cdot E_{kin}^{P_3}}{v_3^2} \Leftrightarrow \tag{1.3}$$

$$m_3 = \frac{2 \cdot U \cdot e}{v_3^2}. \tag{1.4}$$

The computed speed $v_3 = 76,122.1 \ m/s$ and the acceleration voltage $U = 600$ V may be used in Equation (1.4) to determine the mass m_3 of particle 3:

$$m_3 = \frac{2 \cdot U \cdot e}{v_3^2} = \frac{2 \cdot 600 \cdot 1.602 \cdot 10^{-19}}{76,122.1^2} = 3.31795 \cdot 10^{-26} \ kg.$$

A mass of $3.31795 \cdot 10^{-26}$ kg divided by a conversion factor of $1.66053906892 \cdot 10^{-27}$ kg/u gives a mass $m_3 = 19.9812$ u. Furthermore, calibrating the abscissa with the known masses for argon and krypton yields Figure 1.6.

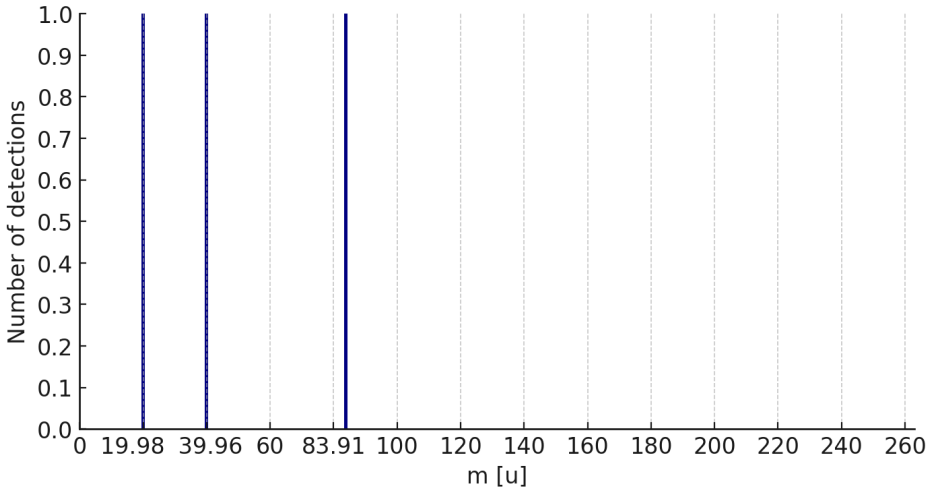

Figure 1.6: Calibrated mass spectrum of situation 2. Contrary to Figure 1.5 the abscissa is calibrated to represent the mass.

Plot 1.6 shows the two known peaks for argon and krypton, as well as a third one on the left. That peak at a lower mass of 19.98 u would seem consistent with the detection of a neon atom (isotope 20) whose mass is 19.992 u. However, the plot twist in this thought experiment 2 is that the experimenter knew from the very beginning that no other rest trace is present in the vacuum chamber of the mass spectrometer, except argon and krypton. Thus, another reason for this lower mass detection must be sought.

The computed mass of 19.98 u is exactly half the value of the argon atom. Nevertheless, the energy of ionisation, often chosen around 70 eV for efficiency (de Hoffmann and Stroobant, 2007), is not enough to break an argon atom in half. Thus, if one knows that only argon and krypton were present in the sample, a particle with a mass of about 20 u can be ruled out. The solution to this puzzling peak might be revealed by the discussion of the ionisation hypothesis of Equation (1.3).

The assumption of single ionisation yielded the following expression for the kinetic energy:

$$E_{kin}^{P_3} = e \cdot U. \tag{1.5}$$

However, a more general way to describe the energy provided by the acceleration voltage is to include the number z of electrons lost by the atom during the ionisation process, with $z = 1, 2, 3, ...$:

$$E_{kin}^{P_3} = z \cdot e \cdot U. \tag{1.6}$$

Equation (1.6) may now be used in Equation (1.3) to compute m_3:

$$m_3 = \frac{2 \cdot E_{kin}^{P_3}}{v_3^2} = \frac{2 \cdot z \cdot e \cdot U}{v_3^2}. \tag{1.7}$$

Dividing both sides of the equation by z gives the following expression:

$$m_3/z = \frac{2 \cdot e \cdot U}{v_3^2}. \tag{1.8}$$

The values previously used in Equation (1.4) are still valid for the right side of Equation (1.8), yielding the same result:

$$m_3/z = \frac{2 \cdot e \cdot U}{v_3^2} = 19.9812\ u. \tag{1.9}$$

Assuming an atom ionised twice for particle 3, *i. e.* $z = 2$, Equation (1.9) becomes:

$$m_3/2 = 19.9812\ u \Leftrightarrow m_3 = 2 \cdot 19.9812 = 39.962\ u.$$

Taking $z = 2$ into account, the computed value for m_3 becomes 39.962 u, meaning the mass of argon. Using the same approach with $z = 1$ for particle 1 and particle 2 leads to the exact same results as previously computed above. Therefore, the correct interpretation of Figure 1.5 is to recognise the detection of one krypton ion Kr^+ at 5.65 μs (simple ionisation), one argon ion Ar^+ at 3.90 μs (simple ionisation), and one argon ion Ar^{++} at 2.76 μs (double ionisation).

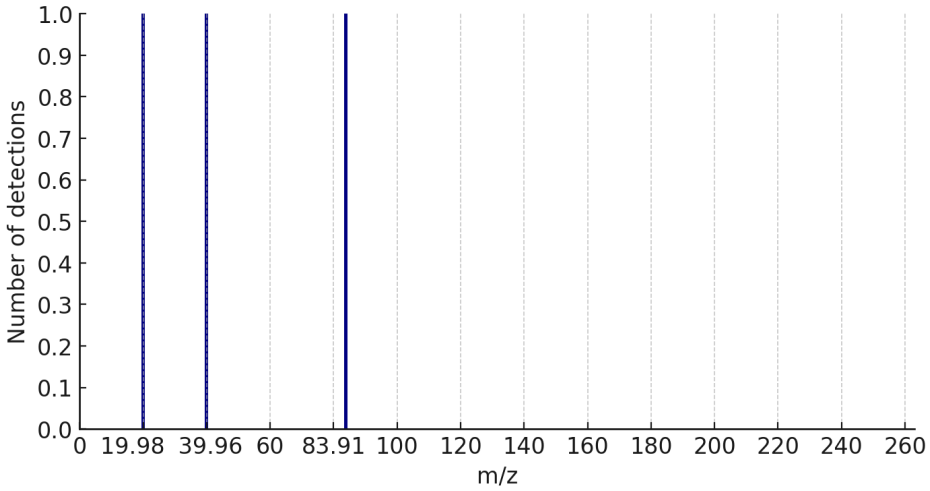

Figure 1.7: Calibrated mass spectrum of situation 2. Contrary to Figure 1.6 the abscissa is calibrated to represent the mass-to-charge ratio, as it is a usual procedure in mass spectrometry.

Equation (1.8) leads to the introduction of the concept of mass-to-charge ratio m/z. Even though single ionisation is the most likely in numerous situations, higher ionisation levels may not be ruled out in mass spectrometry. As a consequence, rather than simply using the mass m in a mass spectrometry spectrum, the abscissa is usually calibrated with the mass-to-charge ratio m/z, as is illustrated in Figure 1.7, while the ordinate shows a quantity related to the relative abundance of the chemical species. The mass, displayed as the relative mass m, and the the number of charges z, both have no unit. Thus, m/z is a dimensionless number.

The thought experiments explained in this section illustrate the main principles of a time-of-flight mass spectrometer. Furthermore, they enable to introduce the so-called mass-to-charge ratio and to show a simplified view of a mass spectrum generated by a mass spectrometer. Therefore, it is demonstrated in the section that the mass-to-charge ratio of the particle may be retrieved from its time-of-flight measurement. The equation used to calibrate a mass spectrum is explained in Section 1.3.2.

1.3.2 Mass Calibration Equation

In the idealistic situation in which all particles are ionised exactly on the same spot and start their travel exactly at the same time that is known without any signal delays, the equation describing the mass-to-charge ratio m/z with regards to the measured time of flight t is of the form:

$$m/z = K \cdot t^2. \tag{1.10}$$

Since $m/z > 0$ and $t > 0$, then $K > 0$ and Equation (1.10) can be rewritten as:

$$\sqrt{m/z} = \sqrt{K} \cdot t. \tag{1.11}$$

Equation (1.11) is valid in an idealistic case. However, in a more realistic situation, there is always a signal delay caused by the electronics of the instrument, the ions do neither start their journey in the ion optics at the exact same position, nor at the exact same time, and they might also carry a slighty different energy. The parameter t_0 accounts for all these time delay effects. Therefore, a mass spectrum must be calibrated using the following equation (de Hoffmann and Stroobant, 2007) with m/z the mass-to-charge ratio and t the measured time of flight:

$$\sqrt{m/z} = C \cdot (t - t_0). \tag{1.12}$$

In Equation (1.12), C and t_0 are two unknown parameters. Consequently, if two masses and their corresponding times of flight are identified in the spectrum, a system of two equations with two unknowns may be solved and the obtained parameter values C and t_0 used to determine the masses of all other peaks from their measured time values. If more than two peaks have known masses, a procedure such as a least-square routine might be used to compute C and t_0.

When the behaviour of the mass spectrometer is not quadratic, more terms for a polynomial might be used with t as a variable or a more advanced function.

1.3.3 Determination of the Mass Resolution

In the ion source of a mass spectrometer particles are ionised on different spot. Furthermore, two exact same particles can be ionised on two slightly different time points. Therefore, those two ions will have two slightly different times of flight, even though they have exactly the same mass. Therefore, the measurement curve is not composed of infinitely thin bars, but rather displays peaks with a finite width, as shown in Figure 1.8.

The larger the time-of-flight difference for a given mass, the wider its corresponding peak. Thus, a broader peak means a larger uncertainty on the determination of the exact mass of the peak. Moreover, if a high peak is too broad, it might hide a close and shorter peak for another mass, which might then become undetected. Consequently, it is important to be able to assess to what extent close peaks in a spectrum are distinguishable. To achieve this goal, the mass resolution or mass resolving power is a spectrum quality quantity defined to be practical to use.

The mass resolution R in this work is defined as:

$$R = \frac{m}{\Delta m} \tag{1.13}$$

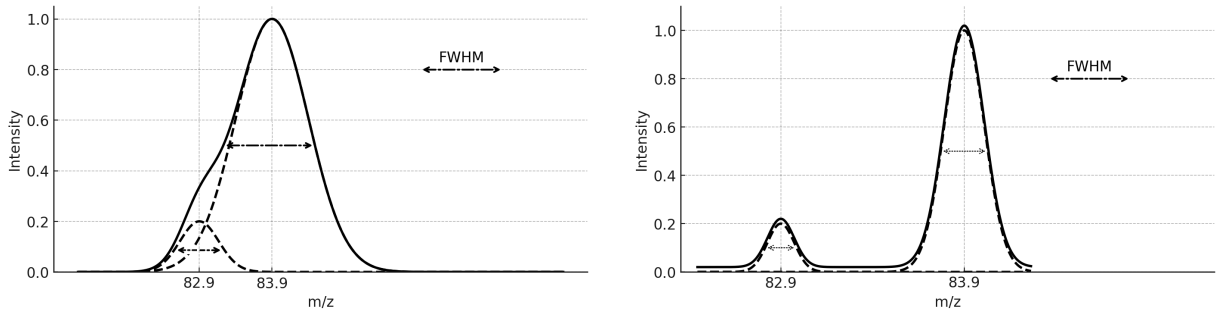

(a) Overlapping peaks, so low mass resolution.

(b) Separated peaks, so high mass resolution.

Figure 1.8: Sketches of realistic mass spectra with the intensity in arbitrary units on the ordinate and the mass-to-charge ratio on the abscissa. Contrary to an ideal view with infinitely thin bars, realistic measurements show a curve whose peaks have a finite width. The blue curves represent each separate contribution of the two different kinds of ions, while the red curves are the cumulated effects measured as the final signal by the mass spectrometer. a) A wide peak around 83.9 u almost completely hides the shorter peak at 82.9 u, while a determination of the precise mass of the tall peak has a large uncertainty. b) The peak at 83.9 u is much thinner, so the shorter peak is clearly detectable, both masses may be more accurately determined, and the relative abundance of one regarding the other given by the areas under the curve might also be more meaningfully estimated. Therefore, mass spectrum b) has a much higher mass resolution than a).

where m is the mass of the considered particles and Δm the corresponding full-width at half-maximum (FWHM). Figure 1.8 also visually shows the FWHM as double arrows across the peaks.

A higher value for R shows that peaks are more separated (relatively low Δm, so thinner peaks), whereas a lower value means the existence of wider peaks, so possibly shorter peaks hidden in tall and broad peaks, hence the lower quality of the spectrum, as in Figure 1.8 a. The analysis of a mass spectrum such as Figure 1.8 b would lead to the conclusion that both isotopes 83 and 84 of krypton are present in the sample with an abundance ratio below 20%.

1.4 Global View of the Instrument

OpenTOF is a scaled-up version of CubeSatTOF and its design adaptation was carried out by Schertenleib (2023) using a simulation software called *SIMION*. Figure 1.9 shows a top view of OpenTOF. The entrance grid of the instrument is represented on the top left corner of the schematic. In space, the direction of flight of the instrument with regard to the investigated atmosphere will be from the right to the left on this schematic. Thus, relatively to the reference frame of the instrument, the fast gas comes from the left and travels to the right in a direction more or less parallel to the dashed line. Next to a series of cylindrical electrodes on its top left, the upper centre of the sketch shows a first drift tube called $D - T_1$, leading to the reflectron on the right. Then, the exit of the reflectron is connected to a second longer drift tubed labelled $D - T_2$ on the lower part of the schematic. Finally, $D - T_2$ ends in front of a detector on the bottom left part of the sketch. A mnemonics for the labelling of the different electrodes follows a logic with this order: the main part of the device is first, then a function of the electrode within that part comes in a second position, and, finally, a last indication is given by a number or a letter if needed. The three main parts of the instrument are represented by Q for the ion source (*Quelle*), DT for the drift tubes, and R for the reflectron. The second part of most of the labels might be *Acc* for acceleration or L for lens.

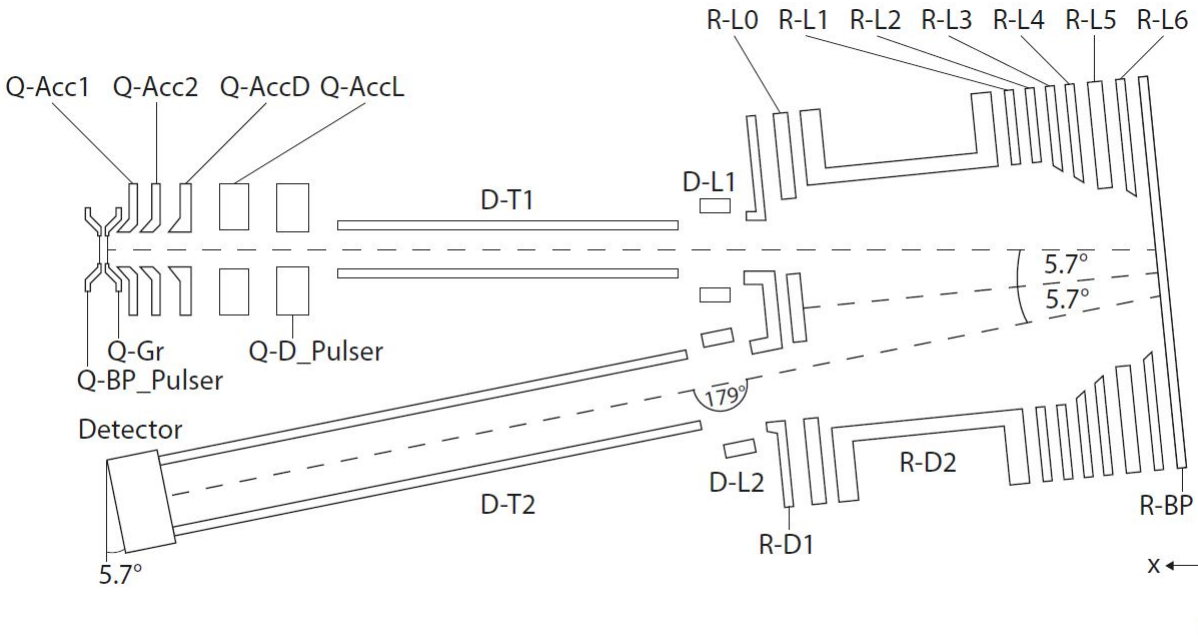

Figure 1.9: Schematic of OpenTOF, as seen from above. A typical size is the distance from Q-BP_Pulser to R-BP, which is about 25 cm.

The two first electrode on the upper left at the entrance of the instrument are two grids: the first is called $Q\_BP-Pulser$ for the keywords Quelle (source), backplane, pulser and the second grid $Q-Gr$, standing for Quelle and ground. The ionisation process takes place between these two grids thanks to an ionisation filament. A pulse of +600 V is applied on $Q\_BP-Pulser$ to push the ions to the right, while $Q-Gr$ is adapted close to 0 V by the operator to fine-tune the mass resolution. Except for the two electrodes with a possible pulse, a specific voltage is supposed to be applied on all electrodes and be kept constant (under normal operation). Once they enter the instrument, the ions are accelerated by successive electrodes with a negative potential: Q_Acc1, Q_Acc2, and Q_AccD. The potential of each of these three electrodes is more negative and Q_AccD has the same potential as the first drift tube $D-T1$. Between Q_AccD and $D-T1$, Q_AccL is set at a different potential to act as an einzel lens to focus the ion beam. The last electrode before the drift tube is called $Q-D\_Pulser$ for source (Quelle), drift, and pulser. The goal of this electrode is to use a pulse to slow heavier ions down and decrease the energy spread, which is necessary for high masses at high velocity (the upper end target being 1000 u at $20km/s$). However, the needed pulser will be delivered by the manufacturer and implemented by the team only at a later stage. Therefore, until the implementation of the pulser, $Q-D\_Pulser$ is set to the same potential as the drift tube.

When they travel inside the drift tube $D-T1$, ionised gas molecules are not accelerated anymore and travel with a constant velocity. Since ions with a lower mass have a higher speed than ions with a higher mass, the less massive particles arrive at the right end of the drift tube first. The two first electrodes after the drift tube of length = 80 mm are $D-L1$ (for drift and lens) and then $R-D1$ (for reflector and drift) the first electrode of the reflector. $R-D1$ is set to the same potential as the drift tube ($D-T1$), while $D-L1$ acts as an einzel lens to refocus the ion beam.

The second electrode of the reflector $R-L0$ (for reflector and lens), which is set below the drift potential (more negative voltage), slightly shifts the beam towards the negative y-direction (left with

reference to ion flight direction) and focuses the beam. Thus, this control over the y-direction helps to achieve a higher detector illumination. The third electrode of the reflectron is long, rectangular, and foreseen to be set close to the drift potential. This large section is the result of seven electrodes from CubeSatTOF's inherited design merged together, thanks to several iterations of the voltage optimisation with the *SIMION* software. The last seven electrodes of the reflectron are $R-L1$, $R-L2$, $R-L3$, $R-L4$, $R-L5$, $R-L6$ (again, R for reflector and L for lens), and the reflector back plane $R-BP$. The purpose of these electrodes is a gradual increase of the voltage to retard and reflect the ions towards the exit of the reflectron. Contrary to the other electrodes, $R-L3$, $R-L4$, and $R-L6$ have bevelled inner edges to increase the homogeneity of the electric field. All electrodes of the reflectron are parallel and its full length is 90 mm. Furthermore, the vector normal to the back plane has an angle in the xy-plane of 5.7° with respect to the symmetrical axis of the acceleration electrodes and the drift tube 1 (which is also the ions' main direction of flight). When exiting the reflectron, the ions fly through the second opening of the electrodes $R-L0$ and $R-D1$.

The last electrode before the second drift tube $D-T2$ is $D-L2$, which acts again as an einzel lens to refocus the beam after its travel through the reflectron. Then, $D-T2$ has a length of 130 mm and is set on the same potential as the first drift tube. Figure 1.9 shows $D-T1$'s mirrored axis of symmetry, which goes through the reflectron exit and which also has an angle of 5.7° with respect to the back plane's normal vector. It is worth noticing that the second drift tube $D-T2$ is not aligned with that mirrored axis of symmetry. Instead, $D-T2$ has an angle of 1° with respect to that line, because of the position of the ionisation filament. Given the x- and y- axes as on Figure 1.9 and a right-hand system of axes, the electron beam is directed along the z-axis (i.e. towards the page). However, the electron beam is placed in the positive y-axis direction 1 mm away from the axis of symmetry of the ionisation chamber to increase the mass resolution, according to simulations by Schertenleib (2023). Thus, the second drift tube is slightly tilted to compensate for the off-centre position of the ionisation filament. Finally, the detector block is mounted at an angle of 5.7° in the xy-plane with respect to the symmetrical axis of the second drift tube. Simulations of the detector performance at 10 km/s and 20 km/s carried out by Schertenleib (2023) showed that the maxima were obtained for an angle with respect to the second drift tube between 4° and 6°. Therefore, the detector is slightly tilted by an angle of 5.7°, taking an orientation parallel to the reflectron back plane.

1.5 Novel Gas Inlet of the Instrument

In current mass spectrometers designed for orbiter or flyby applications, the particle flux to be analysed is handled either by a closed source system or an open source system Fausch et al. (2022a). Closed source systems use a thermalising chamber, as illustrated in Figure 1.10a. After entering the so-called antechamber through a slit, the fast molecules rebound several times on the walls, loosing their kinetic energy step by step, until they reach a much lower energetic state and then enter the ionisation section. Once ionised, they are accelerated thanks to an electrical field to be sent inside the ion optical system. The pressure due to the gas flow in the antechamber increases the density of the gas, leading to a higher sensitivity of the instrument. Furthermore, another advantage is that the mass spectrometer may deal with a large range of velocities. The disadvantage, however, are the possible chemical changes or the fragmentation caused by the impacts with the walls resulting in more complex mass spectra. Therefore, this altered mix of particles might prevent the information about the initial parent molecules or the abundances to be correctly retrieved.

A classical open source entrance is depicted in Figure 1.10b. The gas molecule, travelling on the schematic from left to right, directly enters the zone in which it is ionised. Then, the ion is deviated

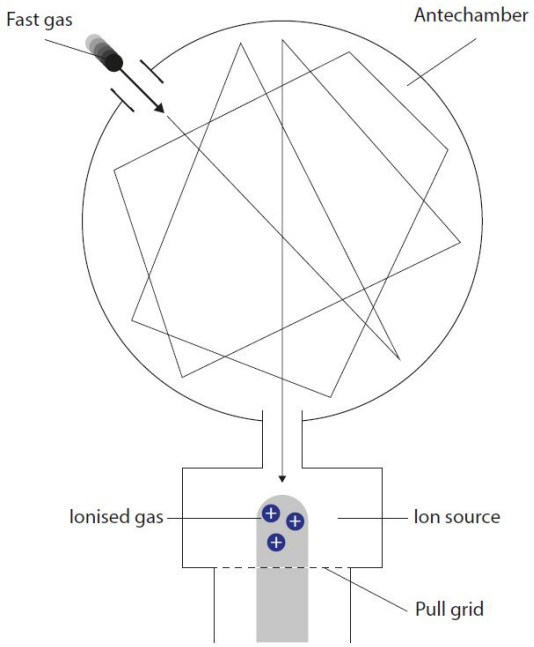

(a) Closed entrance.

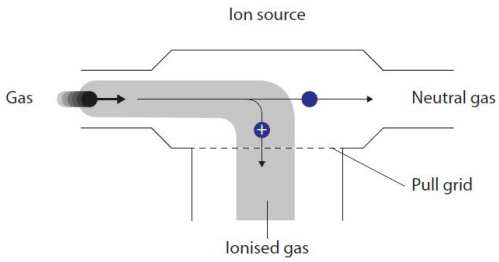

(b) Open entrance.

Figure 1.10: Schematic of two different inlet for an ion source. These two kinds of system are often used for space applications, but it is not the case for OpenTOF. (a) A closed ion source system. (b) A usual open ion source system.

from its initial trajectory thanks to a strong electrostatic field to end up with a velocity directed towards the mass analyser of the instrument (downwards on the schematic). Thus, this technique has the advantage of hindering gas alteration, since no collisions with the walls are needed. However, the higher the speed, the stronger the electric field has to be, hence the need for a high voltage on the pull grid. Moreover, the highest available voltage has an upper boundary for practical aspects, mainly to prevent electrical discharges and to restrict the consumed power. Consequently, such an open entrance system is often limited to maximal speeds of 5 km/s (**?**), as for the Neutral and Ion Mass Spectrometer (NIM) on board the Jupiter's Icy Moons Explorer (JUICE) spacecraft (Föhn et al., 2021; Lasi et al., 2020).

The team working in the Unit for Space Research and Planetary Sciences at the University of Bern designed a novel system without the disadvantages of the closed source or of the classical open source. This special entrance system is called a Direct Open Source (DOeS) and is depicted in Figure 1.11 (**?**). The fast and neutral gas molecule moves towards the entrance grid, the push grid, which is called $Q-BP\_Pulser$ on OpenTOF. Then, the neutral molecule enters the ionisation zone in which an electron beam is directed perpendicularly to the system's main axis of symmetry, which is more or less along the direction of the incoming gas. The next grid, the static grid, is labelled $Q-Gr$ on OpenTOF. After ionisation, the fast particle is pushed out by the pulsed voltage on $Q-BP\_Pulser$, passes $Q-Gr$, and is accelerated towards the mass analyser.

The main advantages of the DOeS design are that no collision alters the gas to be studied and the allowed flyby velocity is much higher than the usual 5 km/s, since no high voltage is needed to completely bend the initial gas trajectory towards the mass analyser. This direct entrance was necessary to enable OpenTOF to measure complex molecules with masses of at least 800 u (even up to 1,000 u for lower velocities) without ambiguity and at relative flyby velocities up to 20 km/s,

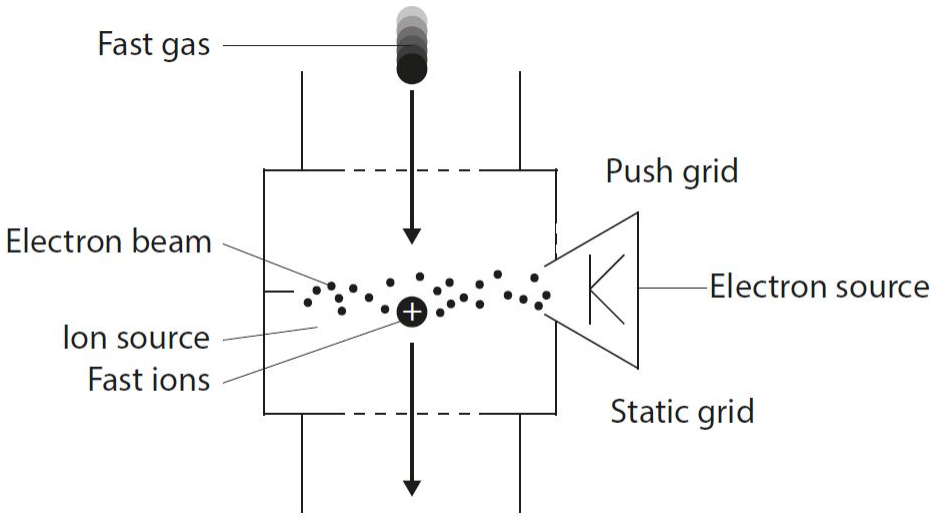

Figure 1.11: Schematic of a Direct Open Source (DOeS). This novel system is used on CubeSatTOF and OpenTOF.

following existing mission concepts, especially to the moons of Saturn and Jupiter (Fausch et al. (2022a) and references therein).

One drawback of the direct open source is the concession on a higher sensitivity, since it is less easy to accumulate ions and prepare large packages with fast particles. However, when sensitivity is still satisfactory, it is a convenient trade-off to overcome the usual velocity upper boundary of 5 km/s and reach 20 km/s (Fausch et al., 2023).

1.6 The Detector Block

Microchannel plates (MCPs), as drawn in Figure 1.12, are flat structures with numerous thin, tubular and parallel holes, whose surface is a layer of semiconductor (de Hoffmann and Stroobant, 2007). For the MCPs used with OpenTOF the straight channels have a diameter of 12 μm and are slanted of about 12° with respect to the vector which is normal to the plate, while the full MCP is 0.6 mm thick and has a diameter of about 25 mm. The voltage applied to one MCP is about 1000 V, but cannot go above 1200 V. Otherwise, the MCP is damaged. Thus, the gain of one MCP at operating voltages is 10^3 to 10^4. Several MCPs may be used in series to create a higher amplification of the signal (Huber et al., 2013). In the case of OpenTOF, two circular MCPs are stacked on top of each other with conductive rings on the edges in front of a spiral anode. Figure 1.12 represents the situation from the side. The two MCPs are directly connected in series, yielding a total resistance of several tens of megohms. The anode is part of a greater circuit (not depicted in Figure 1.12), while not being directly connected in series with the MCPs. A voltage of the order of magnitude of approximately 2000 V is applied between the MCP front (MCP-F) and the MCP back (MCP-B), yielding a total gain with an order of magnitude of 10^6 (10^8 if the maximal voltage of 2400 V is applied).

The principle of a detector with MCPs is shown in Figure 1.12. An ion if travelling towards the top MCP's front side. The trajectory is represented as towards, i.e. more or less perpendicularly to the MCP surface. Once it hits the wall of a microchannel, the ion causes secondary electrons to be released. Each of these electrons is then accelerated thanks to the voltage across the MCPs

(the potential at MCP-B is higher than at MCP-F). Thus, this electron collides with the wall of the channel deeper within the MCP, therefore releasing more secondary electrons on a trip further down the microchannel. This process of repeated collisions and release of more electrons after each collision leads to an avalanche effect during which a single charge coming onto the MCP can cause 10^3 – 10^4 charges to leave it (de Hoffmann and Stroobant, 2007; Huber et al., 2013). Consequently, the electron avalanche is responsible for the charge amplification gain.

A higher voltage across the MCP means a higher gain. However, above a given value the avalanche effect in the MCP is saturated and a maximal value for the gain is reached. Moreover, an MCP also has a maximal electric tension it can withstand before being damaged, hence the usual values of 1000 to 1200 V for the voltage across the MCP and 10^3 to 10^4 for the corresponding gain. Finally, if two MCPs are stacked, the released secondary electrons of the first MCP will trigger avalanches in the second (de Hoffmann and Stroobant, 2007; Huber et al., 2013). Therefore, a total gain of 10^6 – 10^8 can be achieved, which is enough to detect a single ions.

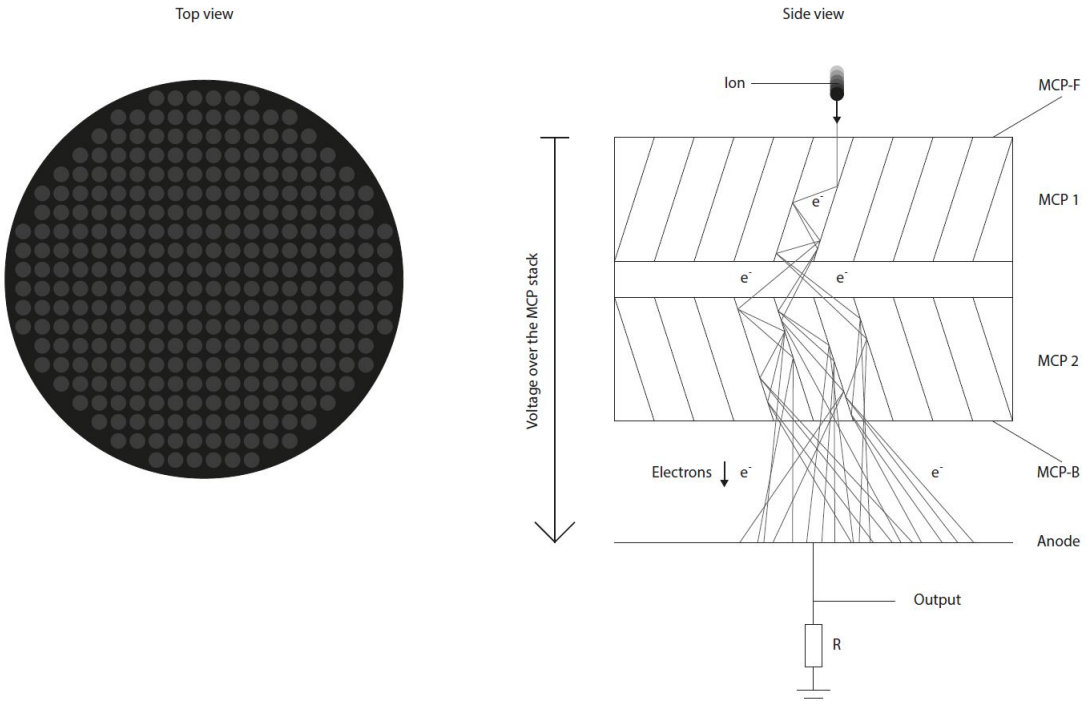

Figure 1.12: Schematic of the microchannel plates (MCPs) and the anode. On the left is a top view, whereas a side view is illustrated on the right.

1.7 Working Principle of the Low Energy Ion Source (LEIS) Equipment

Low Energy Ion Source (LEIS) is a device designed and built in-house at the Unit for Space Research and Planetary Sciences in Bern. Figure 1.13a displays a two-dimensional schematic of the LEIS, in which full lines are flat plates or electrodes and grids are represented by dashed lines. The top of the diagram shows a filament made out of tungsten. When a voltage is applied to this tungsten wire an electric current flows though it, therefore heating the wire. Thus, electrons are emitted from the wire as a consequence of thermionic emission (Fausch et al. (2024) and references therein).

The first electrode, called the extraction grid, helps electrons to be given off by the emission wire and accelerates them towards the ionisation zone (downwards on the diagram). The ionisation box, named ion box, is a group of five electrodes forming a cuboid volume, which are all electrically connected to one another. The ion box exit grid, seen on the right of Figure 1.13a, acts as a sixth side closing the ionisation volume. However, the ion box exit grid is electrically insulated from the ion box. Furthermore, the full volume is not hermetically sealed from the rest of the vacuum chamber, since gas can flow in and out of the ionisation volume and of the full LEIS. Electrons emitted by the cathode can be attracted by the potential inside the ion box, due to the voltages applied to the ion box and the ion box exit grid. Consequently, an electron beam forms at the wire and is directed downwards through the ion box, the electron collector grid and falls onto the electron collector, the last electrode at the bottom of the schematic. If gas is let into the ion box from the left side, some electrons will interact with the gas and ionise it. The positive ions are slowly moved towards the right thanks to a slight potential difference between the ion box and the ion box exit grid, before being pushed out of the LEIS. Most of the acceleration given to the ions is controlled by the potential difference between the ion box exit grid and the housing (which is generally set to ground). Therefore, an ion flux travelling from left to right is generated by the LEIS, with velocities up to 20 km/s and beyond. A picture of the LEIS is also given in Figure 1.13b.

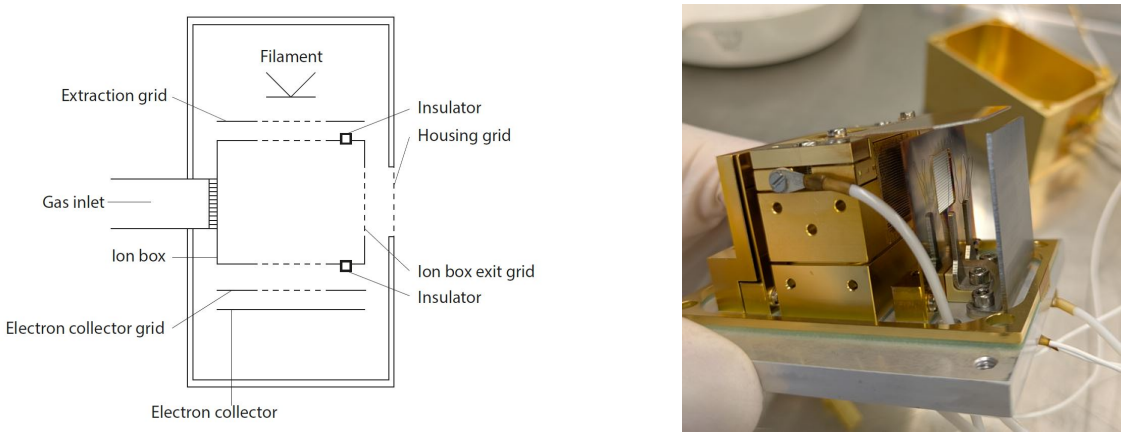

(a) Schematic of the LEIS.

(b) Picture of LEIS 4, the current version.

Figure 1.13: The low-energy ion source (LEIS). (a) Two-dimensional schematic of the LEIS as seen from above through the housing. Electrodes are represented by full lines, while grids are depicted thanks to dashed lines. (b) Picture of the current version of LEIS without its housing. The filament and the extraction grid are visible.

1.8 Working Principle of the Conversion Surface

The device named *conversion surface* or interchangeably *neutraliser* throughout this work is used to convert ions into neutrals and was also designed and built in-house, as LEIS (Rubin et al., 2006; Sokół et al., 2024). The device, represented in Figure 1.14 and photographed in Figure 1.15, is mainly made of a silicone wafer with a gold layer coated on its slightly curved top surface. This top surface acts a charge-state conversion surface. A flux of ions, e.g. generated by the LEIS, is shot from the rear side (left in Figure 1.14) at a grazing angle with respect to the top surface. After interacting with the surface, some ions will catch an electron and become neutral, but will still leave the front end of the conversion surface with a similar speed as when they were ions. The surface being

connected to ground or to a picoampermeter, electrons are renewed in the surface. Furthermore, if the electric current is measured by a picoampermeter, information about the number of ions being converted might be estimated. Eventhough a non-negligible portion of the ion flux might not be converted and stays ions, the combination of the LEIS and the neutraliser has the ability to create a flux of high-velocity neutral gas. Therefore, the coupling of LEIS and the conversion surface was experimented, since the development of a testing facility reaching velocities up to 20 km/s and beyond is necessary to test and calibrate OpenTOF, the Neutral gas and Ion Mass spectrometer (NIM) on board the JUICE spacecraft (Föhn et al., 2021), or any other instrument flying at high velocities with respect to its target.

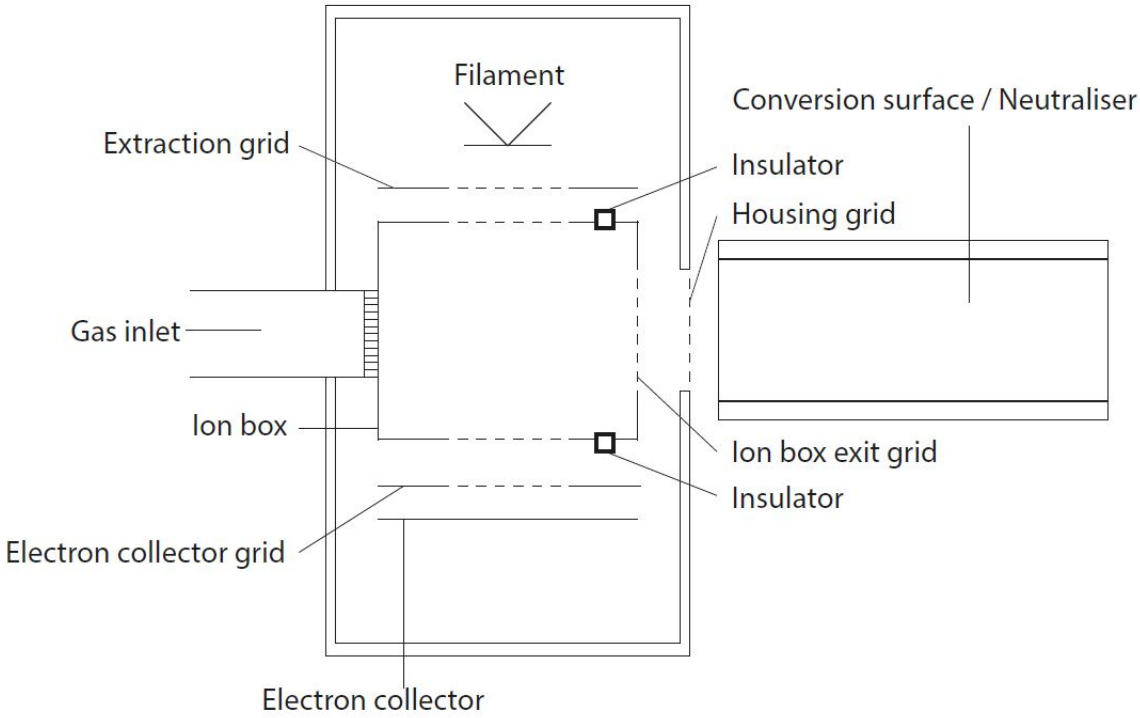

Figure 1.14: Schematic of the conversion surface with LEIS as seen from above.

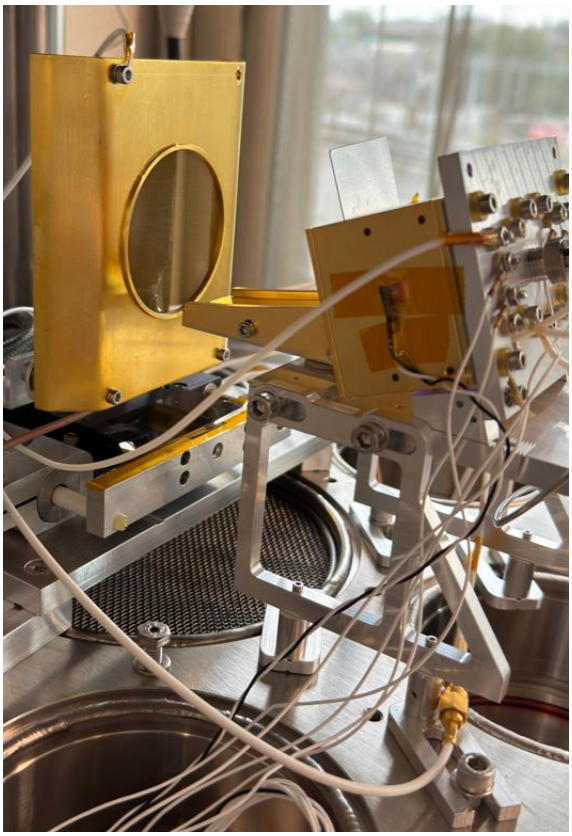

Figure 1.15: Picture of the conversion surface with LEIS in front of a circular grid (Faraday cup 2).

Chapter 2

Low Energy Ion Source (LEIS)

The LEIS testing equipment is an in-house device designed to generate ions, focus them, and accelerate them to form a beam of ions to verify mass spectrometers. It is an essential ground testing equipment. Thus, LEIS is different from the ion source within a mass spectrometer, such as OpenTOF. Moreover, the schematic diagram of the LEIS and its working principle are explained in Section 1.7. This chapter explains the tests carried out to prepare and optimise LEIS for mass spectrometers, namely for OpenTOF in the first place, discusses the results that led to the choice of filament diameter, and shows a beam characterisation of the device.

2.1 Setup for the LEIS Wire Testing

Carbon nanotubes were used in a previous version of LEIS, but their production was discontinued. Thus, it was decided to switch the electron emitter to a tungsten wire (Fausch et al., 2024). Tungsten wires are hot emitters and, therefore, higher temperatures imply a higher energy spread. The energy spread of ions generated by LEIS is measured and discussed in Section **??**. Three wires made out of the same material, i.e. tungsten, and with the approximate same length of 50 mm were tested. However, each wire had a different diameter: 0.20, 0.15, and 0.10 mm with a conservative uncertainty estimation of $\pm$ 0.01 mm. These dimensions were based on previous experience of the research unit in Bern (Fausch et al., 2024). The wires were tested from the thickest to the thinnest. The LEIS was installed in a small vacuum chamber using a turbomolecular pump reaching a typical pressure of $2 - 4 \cdot 10^{-8}$ mbar. A picture of the vacuum chamber can be seen in Figure 2.1. Inside the vacuum chamber, LEIS was installed in front of a Faraday cup at a distance of 10 mm, as illustrated from above in Figure 2.2. During electron emission at the cathode, missing charges in the wire are replaced by electrons coming from the bias voltage. Thus, an amperemeter was included between the bias voltage source and the filament power source to display the cathode's electron emission current. The LEIS configuration presented in Section 1.7 is the final setup of the version 4 of the device. However, the first wire with a diameter of 0.20 mm was tested with a series of ion-focusing rings, before they were removed and replaced by the current ion box and ion box exit grid. The reason for this change is explained in Section 2.2.3. The ion-focusing rings are a series of conducting rings attached together and placed parallel to one another, with their centres aligned with the centre of the LEIS output opening. Resistors connect every ring to the next one. The potential of the rear ring is foreseen to be the same as the one that would be applied to the ion box, while the front ring plays the same role as the ion box exit grid.

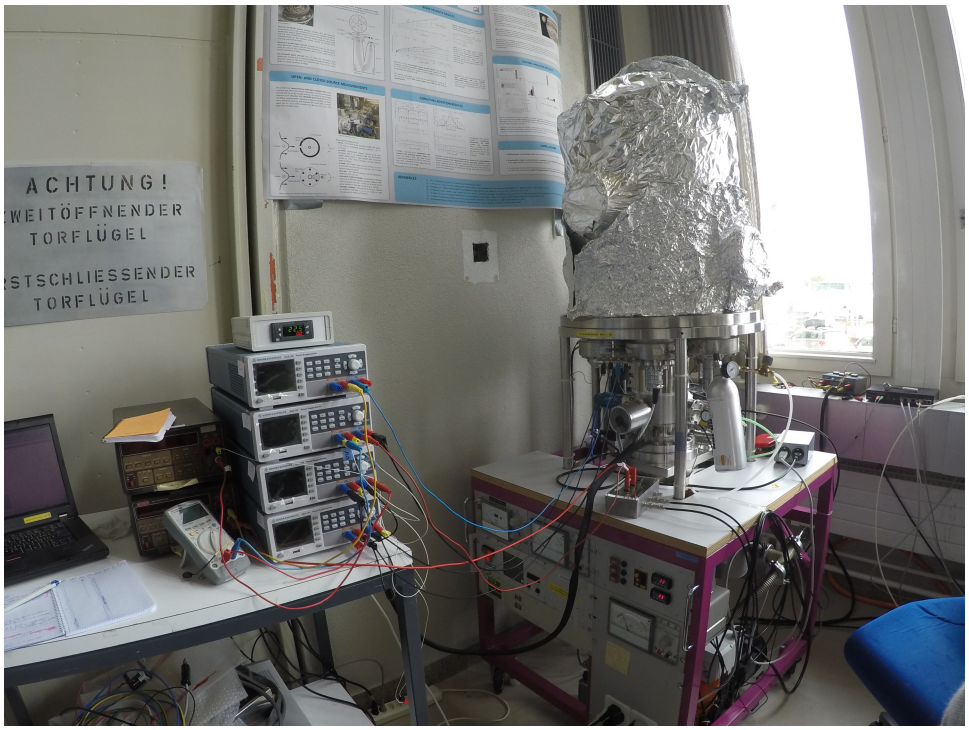

Figure 2.1: Picture of the vacuum chamber before the LEIS filament testing. Notice the multimeter for scale. Four power supplies, two amperemeters, and a multimeter are connected to the vacuum chamber.

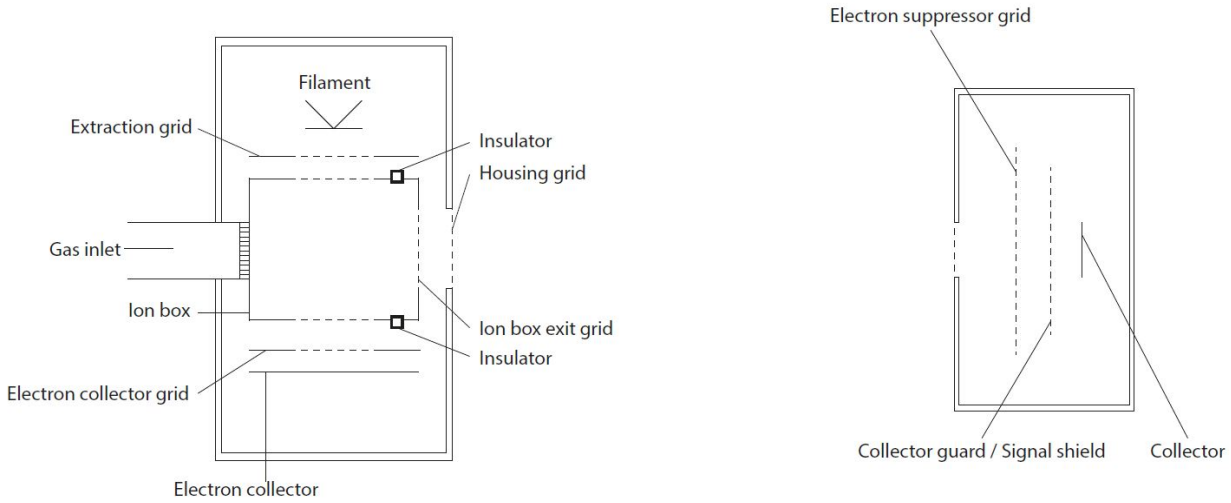

Figure 2.2: Schematic of the setup for the LEIS wire testing. LEIS is on the left, while the Faraday cup is on the right. Dimensions are not to scale since the devices have a width of a few centimetres and the distance between them was only 10 mm.

2.2 Electron Emission Stability of LEIS

The goal of LEIS is to generate an ion beam at specific velocities that can be used to calibrate mass spectrometers. If the electron emission at the cathode of LEIS is unstable, then the ion generation

will dynamic, whereas the optimisation process calls for a comparison of measurements carried out in similar conditions. Therefore, the first necessary requirement on LEIS is a stable electron emission at the cathode of at least two hours. This section explains the results of the tests carried out to decide what diameter to choose for the tungsten wire and what settings to use when operating the LEIS equipment. Experience shows that a wire length of about 50 mm typically fills the ionisation volume with sufficient electrons for ionisation, whilst preventing space charge (Fausch et al., 2024). Three possibilities for the diameter were investigated, namely 0.20, 0.15, and 0.10 mm with an uncertainty of ± 0.01 mm.

2.2.1 First Use of the Filament with a Diameter of 0.20 mm

During the first attempts to use the 0.20 mm wire, an electron emission current of only a few μA was achieved. Furthermore, the electron emission was unstable, with rare but possible sudden bursts up to 1638 μA. Starting at a room temperature of about 22 °C, the housing of LEIS reached temperatures between 50 °C and 70 °C, sometimes with a temperature increase rate of about 0.4 °C/min. The temperature of the wire itself, which was approximatively inferred from resistivity using recommended values by Desai et al. (1984), even reached about 2465 °C. High temperatures were reached since approximately 10 W were needed and the cathode temporarily became out of use after attempts to reach 137 μA. Eventually, the resistance of the emission cathode oscillated between 40 Ω and values exceeding measurement limits of the ohmmeter. Therefore, the cathode was considered unsuitable and LEIS had to be repaired. The wire holder contains polyether ether ketone material. The temperatures inside LEIS were considerably higher than displayed by the housing sensor, such that the PEEK support was bent. Thus, the cathode was disconnected causing a drastic increase in resistance and a rapid cathode failure. Therefore, LEIS had to be refurbished.

2.2.2 Results of the Emission Stability for 0.20 mm

After the first series of tests, the faulty PEEK support in the LEIS equipment was replaced. Furthermore, the wire holder was attached slightly closer to the extraction grid. Thus, the filament was then only approximately 3 mm away from the extraction grid to aim for a higher electron extraction at a given power used in the wire. Finally, the ion-focusing rings and the same filament with a diameter of 0.20 mm were kept to continue the tests. The power supply was set to constant voltages. The tests were carried out without gas added in the vacuum chamber, so with a starting pressure in the range of about $(2 \text{ to } 4) \cdot 10^{-8}$ mbar for a starting temperature close to a room temperature of 22 °C.

Measurements 1 for a Diameter of 0.20 mm

The cathode ramp-up rate was +0.1 V per 30 s. Until 14 minutes at a voltage of 2.8 V, a current of 2.33 A, and a power of about 6.5 W no electron emission was measured, as shown in Figure 2.3. After 14 minutes, with 2.9 V, 2.38 A, and approximately 6.9 W, the electron emission began to be detected. After 19 minutes, the ramp-up ended at 3.8 V, 2.80 A, and about 10.6 W to reach an electron emission of 14.6 μA. During the next 31 minutes the electron emission slightly increased to reach 15.0 μA, but the maximal value difference still stayed below 3 %. The electron emission slowly decreased by about −2.2 μA/h, i.e. −14.9 % after an hour. Then, 101 minutes after the electron emission reached 14.6 μA, it strongly decreased with a rate of almost −8 μA/h (−3.9 μA in 30 minutes). There was a slightly less strong decrease down to an electron current of 4.5 μA 226 minutes after the end of the ramp-up. The final temperature of the LEIS housing was (87.8±0.1) °C after (245 ± 1) minutes of use.

The needed power of about 10 W was high compared to usual values of conventional filament, which are rather closer to 1 W (Fausch et al., 2024). The consumed power is not a problem for available energy, since LEIS is a ground testing device. However, a high power leads to issues regarding high temperatures within LEIS. The electron emission of 14.6 μA was low (Rubin et al., 2006). As a comparison, in conventional ion sources the range usually reaches 100 to 1000 μA (Fausch et al., 2024; Föhn et al., 2021). For an optimisation session of 2 to 4 hours with a mass spectrometer, the obtained electron emission was found not to be stable enough. The average temperature increase rate on the housing was approximately +15.5 °C/h which is quite high, but understandable, since more than 10 W were used. Such a high temperature outside of the LEIS housing of almost 90 °C means that the area close to the wire inside was even much hotter. The cathode temperature estimated by the resistivity of tungsten was about 2421 °C, using recommended values by Desai et al. (1984).

Measurements 2 for a Diameter of 0.20 mm

Measurement 2 is shown in Figure 2.3. The ramp-up rate was +0.1 V per 15 seconds during 9 minutes to reach a first emission level of 2.5 μA at a voltage of 3.6 V, a cathode current of 2.73 A, and a power of about 9.8 W. At 14 min 45 s, the voltage was increased from 3.6 to 4.0 V, with a wire current of 2.9 A and an approximate power of 11.6 W, thus yielding an electron emission of 9.2 μA. Then, at 18 minutes, the voltage was increased to 4.5 V with a current of 3.12 A, an approximate power of 14 W, and a mean electron emission of 35.4 μA with a standard deviation of $\sigma = 0.5$ μA. At 24 minutes, the voltage was increased to 4.7 V with a current of 3.20 A, an approximate power of 15 W, and an electron emission of 57.6 μA with $\sigma = 0.3$ μA. At 31 minutes, the voltage was raised to 4.9 V with a current of 3.27 A and a power of about 16 W, yielding a mean emission of 92.5 μA with a standard deviation $\sigma = 0.1$ μA. At 36 minutes, the cathode voltage was finally set to 5.0 V with a current of 3.31 A and a power of approximately 16.6 W to generate an electron emission of (115.9 ± 0.20) μA. Then, the voltage was shortly set down to 4.8 V and 4.9 V for 5 minutes each, to test if the electron emission would decrease previously measured values. After that short successful test, the voltage was raised again to 5.0 V with a same current of 3.31 A, yielding a starting electron emission of (116.0 ± 0.1) μA at 51 minutes, degrading to (105.4 ± 0.1) μA at 90 minutes and (103.1 ± 0.1) μA at 95 minutes even though the cathode voltage and current stayed constant. The housing temperature reached 73.6 °C in 90 minutes.

The power consumption of about 16.6 W was high. Thus, the average temperature increase rate on the LEIS housing was +33.8 °C/h. A higher electron emission of approximately 116 μA was achieved in measurement 2 compared to the previous measurement 1 displayed in Figure 2.3. After the short test with 4.8 V at 41 minutes, the electron emission for 4.9 V and 5.0 V were similar to values before 41 minutes. After the cathode was finally set to 5.0 V with a high power of 16.6 W, the decreasing rate of the emission was -17.6 μA/h, meaning a difference of -15.2% after an hour for a starting emission of 116.0 μA. The power needed was the reason for the high wire temperature of 2631 °C inferred from values recommended by Desai et al. (1984). With a possible difference of more than 30 % in only 2 hours, the electron emission might have not been satisfactory enough for an optimisation session with a mass spectrometer. The current achieved was already in the usual range of (100 to 1000) μA for mass spectrometer ion sources (Fausch et al., 2024; Föhn et al., 2021), but stayed low and required a high power.

Measurements 3 for a Diameter of 0.20 mm

Measurement 3 is shown in Figure 2.3. The cathode voltage was raised from 0 to 4.1 V with steps of 0.1 V per 10 s. Then, an emission current of approximately 10 μA was kept for a few minutes

just to verify if the emission looked stable for this short period. Then, the cathode voltage was increased by steps of 0.1 V per minute to reach 4.8 V and 3.22 A with a power of about 15.5 W). Therefore, at the end of the ramp-up after 22 minutes the emission was (57.8 ± 0.1) μA and slowly increased to a top level of (59.9 ± 0.1) μA in 48 minutes, under the same voltage and current. About 60 minutes after the end of the ramp-up, the electron emission started decreasing down to a final value of (53.6 ± 0.1) μA at 155 minutes. The mean value of the electron emission was 58.1 μA with a standard deviation of $\sigma = 1.97$ μA and the highest difference between the starting emission of (57.8 ± 0.1) μA and any value during the 133 minutes of use after ramping-up was (4.2 ± 0.2) μA which represented less than 8 %. The temperature on the LEIS housing reached (96.1 ± 0.1) °C in (155 ± 0.25) minutes.

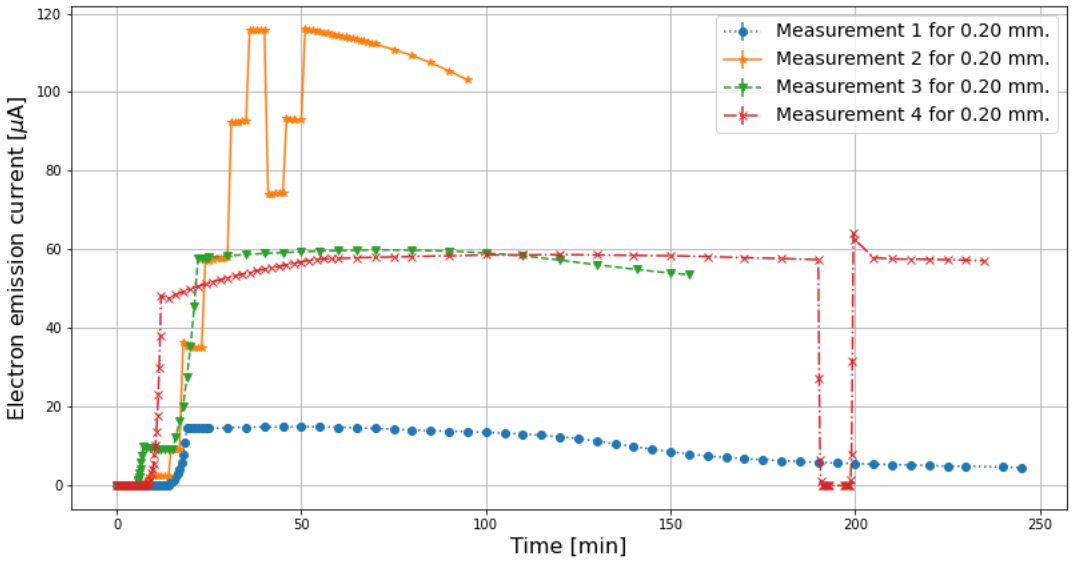

Figure 2.3: Measurements 1, 2, 3, and 4 for the filament with a diameter of 0.20 mm showing the electron emission current as a function of time.

The electron emission was more stable in the first hour than in the second for measurement 3. However, even with the emission decrease in the second hour, an overall maximal difference below 8 % was reached, which was more satisfactory than the first measurement shown in Figure 2.3. If such a behaviour was repeatable, then the stability of the electron emission could be promising to be used with a mass spectrometer for two hours. Even though the mean emission current of 58.1 μA with $\sigma = 1.97$ was higher than the current of measurement 1 in Figure 2.3, it was still low compared to the usual 100 to 400 μA. The needed power of approximately 15.5 W was high, which led the cathode to reach an estimated temperature of 2602 °C with the values recommended by Desai et al. (1984). The temperature of 96.1 °C on the housing was high and the high average temperature increase rate of +28.3 °C/h showed that the continuous use of the LEIS in this configuration must to be limited in time.

Measurements 4 for a Diameter of 0.20 mm

Measurement 4 is shown in Figure 2.3. The tungsten wire was ramped up from 0 to 4.8 V with steps of 0.1 V per 15 s, while the extraction grid was kept at 0 V. Thus, at 14 minutes, the cathode voltage of 4.8 V caused the current to be 3.17 A with a needed power of about 15.2 W. Under these conditions the electron emission current was (47.6 ± 0.1) μA, the approximate resistivity was $7.93 \cdot 10^{-7}$ Ω·m, and the resulting wire temperature estimation was 2636 °C with values recommended by Desai et al. (1984). Afterwards, the cathode settings were kept at 4.8 V and 3.16 A with about 15.2 W), while the voltage on the extraction grid was raised by +25 V every 2 minutes until +500 V was reached at 54 minutes. The cathode settings were still identical, but the electron emission was higher: (57.5 ± 0.1) μA. Then, from 54 minutes until 190 minutes, under the same conditions, the mean electron emission current was 58.09 with standard deviation of $\sigma = 0.41$. Then, the cathode was ramped down to 4.5 V, 4.0 V, 3.5 V, 3.0 V, ..., 0.5 V, and 0 V with one step every 15 seconds. The cathode was switched off for 4 minutes and then ramped up again with the same voltage and time steps but in the reverse order. At 4.8 V with 3.18 A and about 15.3 W a peak with an emission of (64.1 ± 0.1) μA appeared. However, in less than 6 minutes the emission was back to (57.9 ± 0.1) μA. Finally, during the last 30 minutes under a cathode voltage of 4.8 and a cathode current of 3.15 A with 15.1 W, the mean electron emission was 57.47 μA with a standard deviation of $\sigma = 0.25$ μA. In that final period, the computed wire resistivity was $7.98 \cdot 10^{-7}$ Ω·m and the corresponding estimated cathode temperature was 2650 °C according the values recommended by Desai et al. (1984). The temperature on the LEIS housing was (99.2 ± 0.1) °C after 190 minutes and the highest temperature reached (102.1 ± 0.1) °C at 215 minutes.

The average temperature increase on the LEIS housing during the first 190 minutes was 23.9 °C/h. The electron emission went from (47.6 ± 0.1) μA to (57.5 ± 0.1) μA only thanks to the extraction grid, since a higher voltage attracts the electrons from the cathode more. However, a high voltage also means more electrons incident onto the grid, hence a reduced transmission of the electron beam. Therefore, a too high voltage on the extraction grid might lead to fewer electron available for ionisation, even if the electron emission at the cathode is high. The optimal value for the extraction voltage varies with all the settings of the LEIS, but could often be close to a few tens of volts.

The standard deviation being used as an estimation for the uncertainty, the electron emission current was (58.09 ± 0.41) μA during 136 minutes, which shows a satisfactory stability for a measurement session with a mass spectrometer such as OpenTOF. After the short ramp-down test, the electron emission quickly went back to (57.47 ± 0.25) μA, which is an encouraging sign for emission consistency and experiment repeatability. However, this electron emission was still lower than the usual range of (100 to 1000) μA and the power needed of 15.2 W stayed high, leading to a high temperature in LEIS.

2.2.3 Effect of a High Temperature on the Hardware

After conducting measurement 4 (Figure 2.3), LEIS suffered again from a failure of the ion acceleration. During a visual inspection of the interior of the LEIS, it became obvious that some gold-coated regions on different electrodes became dark, likely due to a coating damage. The damage was even stronger on the acceleration rings inside the ion box. Furthermore, the rings lost their parallel alignment, since one side of the tubular shape was squeezed, as shown in Figure 2.4. This damage was attributed to a prolonged high temperature and to an exposure to the electron beam. Therefore, the emission wire was changed for a thinner cathode with a diameter of 0.15 mm, but still with a length of approximately 50 mm, so lower currents, voltages, and powers could be used. The filament's position has been slightly changed by a few millimetres to be now only 3 mm away from the extraction grid. The acceleration rings were removed and the temperature sensor was placed on the

extraction grid on the side of the rings, instead of outside the LEIS on its housing.

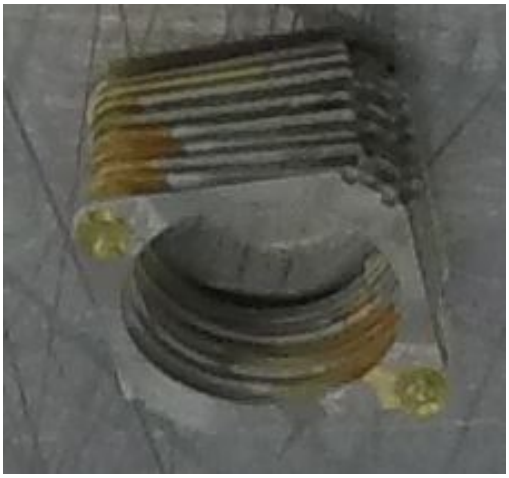

(a) Top view of the ion-acceleration rings.

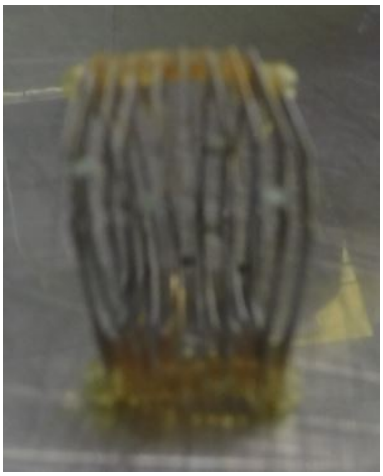

(b) Side view of the ion-acceleration rings.

Figure 2.4: Damage on the ion-acceleration rings due to a high temperature during the tests of the filament with a diameter of 0.20 mm. (a) Top view through the tubular structure. The golden coating was almost removed everywhere (b) Side view. The edge shown above is longer than the other below, because the structure is bent.

2.2.4 Results of the Emission Stability for 0.15 mm

The ion-focussing rings in the ion source of LEIS were taken out, leaving an empty space in the LEIS housing due to the absence of the ion acceleration grids, since it was not necessary at the time for an electron emission characterisation. Thus, the temperature sensor was placed inside LEIS, since sufficient space was available on the extraction grid on the side of ionisation zone, not next to the filament. Furthermore, the cathode was changed to a tungsten wire with the same length of about 50 mm, but with a diameter of 0.15 mm instead of 0.20 mm. A thinner wire with the same length needs a lower power to reach the same temperature. Giving less energy to the system in the same amount of time in turn causes the temperature of the LEIS to rise less than with a thicker wire. All measurements with the 0.15 mm wire were carried out with 0 V on the cathode backplane, -70 V as the filament bias, and $+200$ V on the extraction grid if not stated otherwise.

Measurements 1 and 2 for a Diameter of 0.15 mm

The first two measurements with the 0.15 mm wire did not provide a satisfactory electron emission current, since the cathode current was limited to 2.0 A by the power supply to protect the wire from an overcurrent.

During the first measurement, a short burst reached values above 34 μA, but it quickly went back down to 3.6 μA in 2 minutes. With a cathode voltage kept at 3.5 V, a current of 1.99 A, and a power of about 7.0 W, the electron emission decayed from 3.6 μA to 0.3 μA in only 11 minutes.

The second measurement showed at 9 minutes a highest value for the electron emission at only 1.4 μA for a voltage of 3.6 V and a current of 1.99 A with an approximate power of 7.2 W. Twenty-six minutes after this peak occurred, the electron emission was at or below 0.2 μA, even though the cathode voltage and current were kept constant. At 125 minutes, the electron emission was only 1.4 μA and the temperature inside LEIS was 117.3 ° C.

Measurement 3 for a Diameter of 0.15 mm

From this measurement on the upper limit for the current through the wire was set to 4.0 A, contrary to the first two measurements. This measurement, carried out with a voltage of 200.0 V applied on the extraction grid, is displayed in Figure 2.5.

The cathode voltage was ramped up by steps of 0.1 V per 15 s until 5.0 V and a cathode current of 2.36 A were reached with power of about 11.8 W. The cathode voltage being kept at the same value, the electron emission current declined from (30.1 ± 0.1) μA to (19.4 ± 0.1) μA in (19.5 ± 0.5) minutes. Then, the wire was ramped up with the same initial pace to a voltage of 6.2 V, with a current of 2.67 A, and an approximate power of 16.6 W, thus yielding an initial electron emission of 110.9 μA at 56 minutes. The voltage on the cathode was kept at this value. From 70 until 130 minutes, the electron emission current reached a plateau whose mean value was 121.3 μA with a standard deviation σ of 1.1 μA. The final temperature inside LEIS after 130 minutes was (214.9 ± 0.1) °C. This temperature cannot be directly compared to temperatures previously measured for the 0.20 mm wire, since the sensor placed on the outside of the housing yields lower temperature than a sensor positioned inside LEIS, closer to the wire.

The mean electron emission of 121.3 μA was slightly higher, but similar to the highest current achieved in measurement 2 with the thicker 0.20 mm filament seen in Figure 2.3, while the consumed power stayed about identical. After the needed voltage was set in the 0.15 mm filament, even though the emission current during the first 15 minutes was continuously increasing, it was stable with a low maximal variation below 3 % during the last 50 minutes. This is too short for a complete optimisation session of 2 to 4 hours with a mass spectrometer, but it might be enough for a shorter

measurement. The time limitation of the possible measurement in that case is due to the high temperature reached in the LEIS, which requires the operator to switch the cathode off to prevent damage of the LEIS.

Measurement 4 for a Diameter of 0.15 mm

This measurement was carried out with an extraction grid voltage of 200 V and is shown in Figure 2.5. The cathode voltage was ramped up by steps of 0.5 V per 30 s, except for the last two steps which were +0.1 and +0.05 V, until 6.15 V and a cathode current of 2.58 A were reached at 7 minutes for a power of about 15.9 W. The cathode voltage being kept at the same value, the electron emission current increased from (109.49 ± 0.1) μA to (129.18 ± 0.1) μA in (83.0 ± 0.5) minutes. From 90 until 180 minutes, the electron emission current reached a plateau whose mean value was 130.2 μA with a standard deviation σ of 0.7 μA. The temperature inside the LEIS after 190 minutes was (230.5 ± 0.1) °C. The last drop in electron emission was intentional. The cathode was set to check if 100 μA could be achieved. The voltage was 6.01 V and the current 2.49 A with an approximate power of 15.0 μA, thus yielding a mean electron emission of 100.55 μA with a standard deviation $\sigma = 0.22$ μA over 14 minutes.

The electron emission current of 130.2 μA reached in measurement 4 was slightly higher, but similar, to that obtained in measurement 3 for the same filament diameter of 0.15 mm. However, the consumed power of about (15.7 ± 0.2) W was slightly lower. The cathode needed about 90 minutes to stabilise, stop its continuous increase, and reach its plateau. Thus, it would mean from a practical standpoint that the wire ramp-up would have to be started early enough, long before the actual beginning of a measurement with a mass spectrometer. Furthermore, the electron emission current was stable enough with a maximal variation of 1.6 %, but only during 100 minutes from time $t = 90$ until $t = 190$ minutes, since the cathode had to be ramped down due to the high temperature reached inside the LEIS. This short time might be long enough for a short to medium measurement with a mass spectrometer. Finally, the electron emission was still in the lower part of the usual range of (100 to 1000) μA and the power needed was still high.

Measurement 5 for a Diameter of 0.15 mm

This measurement was carried out a few hours after measurement 4, after the LEIS had cooled down from (233.0 ± 0.1) °C to $(104.8° \pm 0.1)$ °C. The goal of this measurement was to check if the emission could be kept by the operator at approximately 200 μA. The extraction grid voltage was still 200 V and the result can be seen in Figure 2.5. The cathode was ramped up with steps of + 0.5 V per 30 s, except for the last step of + 0.44 V, until the voltage reached 6.44 V and caused a current of 2.58 A to flow through the wire with power of about 16.6 W at 7.5 minutes. The cathode voltage was corrected twice: once at 14 minutes with 6.41 V, 2.57A, and about 16.5 W and a second time at 30 minutes with 6.40 V, 2.57A, and approximately 16.4 W. After the end of the ramp-up, given the two voltage corrections during the cathode operation, the electron emission current was maintained at a mean value of 203.33 μA with a standard deviation of 2.74 μA during (52.5 ± 0.5) minutes. The final temperature inside LEIS was (223.1 ± 0.1) °C.

The mean electron emission current of 203.3 μA was the highest reached at the time and it was in the aimed usual range of (100 to 1000) μA. Furthermore, the consumed power of about 16.5 W was only slightly higher than for the previous measurement with 130.2 μA. With the two cathode voltage corrections needed within 30 minutes, the system had the ability to provide an electron emission with a maximal variation of 4.3 %. Thus, the electron current was stable enough, but only during about 45 minutes, again due to limitation on the allowed temperature of the system. Therefore,

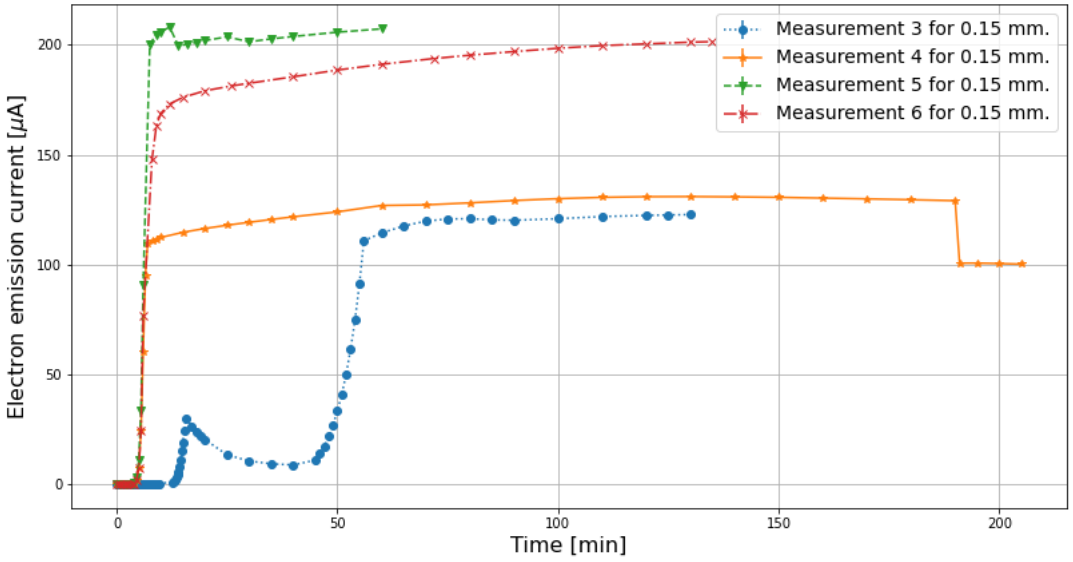

Figure 2.5: Measurements 3, 4, 5, and 6 for the filament with a diameter of 0.15 mm showing the electron emission current as a function of time.

this configuration of the LEIS was not practical for operation, because of the needed corrections. Furthermore, the achieved electron emission was too brief for a long optimisation session with a mass spectrometer, but acceptable for a short measurement.

Measurement 6 for a Diameter of 0.15 mm

This sixth measurement, whose extraction grid voltage was 0 V, is illustrated in Figure 2.5. The cathode voltage was ramped up by steps of 0.5 V per 30 s until a voltage of 6.0 V was reached. Then, at 8 minutes, the voltage was raised to 6.39 V, leading to a cathode current of 2.54 A with an approximate power of 16.2 W and an electron emission of 148.0 μA. The filament voltage was kept at (6.39 ± 0.02) V and the current through the filament stayed at (2.55 ± 0.01) A. However, the electron emission current continuously rose to (201.46 ± 0.1) μA at 135 minutes. Therefore, from 15 until 135 minutes the electron emission had a mean value of 191.43 μA with a standard deviation of 8.69 μA. The temperature inside LEIS was (226.6 ± 0.1) °C after 135 minutes. At that time the current measured on the extraction grid was about 0 A, whereas a potential of +15 V on the extraction grid caused an electron emission of (204.42 ± 0.1) μA with a current on the extraction grid of about (30 ± 10) μA. Furthermore, another try with +200 V on the extraction grid caused an electron emission of (227.5 ± 0.1) μA with a current on the extraction grid of about (190 ± 10) μA. These extra tests with different values for the extraction grid potential between 0 and +200 V are not represented in Figure 2.5, but they were carried out with the same cathode settings as at 135 minutes during 50 more minutes. Consequently, the interior of the LEIS even rose up to (237.6 ± 0.1) °C at 185 minutes.

After 90 minutes, the aim for an electron emission close to 200 μA was achieved with a needed power of about 16.3 W, similar to measurement 5 with the same filament diameter of 0.15 mm. However, only the last 45 minutes were stable with a mean emission of 199.7 μA and a maximal

measured variation below 2.4 %. The electron emission current from 15 until 135 minutes had a maximal measured deviation of 14.5 %, which pointed towards the necessity of an early ramp-up before any measurement with a mass spectrometer, as shown with the previous measurement 5. The temperature inside LEIS was still a limiting factor, but a continuous use from 90 until 185 minutes with a mass spectrometer was possible, since the electron emission stayed stable enough during that time. The possible 45 (to perhaps 90) minutes of end stability is not enough for a long optimisation session, but is satisfactory for a shorter measurement with a mass spectrometer. These tests show that for a given cathode bias, even though a higher extraction potential causes a higher electron emission current, fewer electrons are available in the ionisation box because most of them fall onto the extraction grid. Therefore, the voltage on the extraction grid is an important parameter to optimise, when a given ion flux is aimed to be generated by LEIS during measurements with a mass spectrometer.

The measurements presented in this Section 2.2.4 already showed an encouraging stability and time range that could be acceptable for a short measurement with a mass spectrometer. However, the consumed power was still high, hence the strong temperature increase rate. After the tests for the filament with a diameter of 0.15 mm were complete, the wire inside LEIS was changed to one with a thinner diameter of 0.10 mm to aim for a lower consumed power.

2.2.5 Results of the Emission Stability for 0.10 mm

During measurements 1 to 5, the ionisation zone in the LEIS was still empty, which means that there was no ion box and no ion box exit grid to accelerate ions out of LEIS. Furthermore, no gas was let in, so the pressure in the vacuum chamber was about $(1.35 - 3.25) \cdot 10^{-8}$ mbar during these measurements. As can be seen in Figure 2.6, the electron emission currents for the first two measurements were not stable at all. This might be attributed to the need of the cathode to clean itself from surface contaminants. These measurements showed that the cathode might be used for almost 6 hours at a time with a power of about 5 W before reaching a temperature of (126.8 ± 0.1) °C in a vacuum.

Measurement 3 for a filament diameter of 0.10 mm, using a power of about 5 W, is displayed in Figure 2.6. With a cathode voltage of 4.6 V and a cathode current of 1.09 A, a mean electron emission of 60.64 μA was reached between 6 and 160 min with a standard deviation $\sigma = 1.12$ μA. This data may be compared to measurement 3 for a diameter of 0.20 mm that needed a much higher power of approximately 15.5 W to reach a similar emission, as seen for in Figure 2.3 emission of 60 μA was low compared to the usual range, but the curve was smooth and the maximal variation between the two most different values was only 5.7%, thus showing a satisfactory stability over 154 minutes, which was enough for optimisation measurements with a mass spectrometer.

During the last part of measurement 3 illustrated in Figure 2.6 the cathode voltage was set to 4.84 V, leading to a current of 1.12 A and a consumed power of about 5.4 W, to increase the electron emission current from 60 to 100 μA. Thus, the mean electron emission reached 99.93 μA with a standard deviation $\sigma = 2.27$ μA, which was low, but still in the usual range of (100 to 1000) μA. The maximal variation between the start and the end electron emission over 32 minutes represented about 6 %. Therefore, the electron emission was not perfectly stable, but at least the decrease was smooth and the measurement at 100 μA was too short to conclude about the possibility to carry out measurements with a mass spectrometer.

For measurement 4, the cathode voltage was set to 5.07 V, with a current of 1.15 A and a power of approximatively 5.8 W, thus yielding an electron emission current between (143.18 ± 0.05) μA at 20 min and (156.34 ± 0.05) μA at 180 min, as illustrated in Figure 2.6. This electron emission was

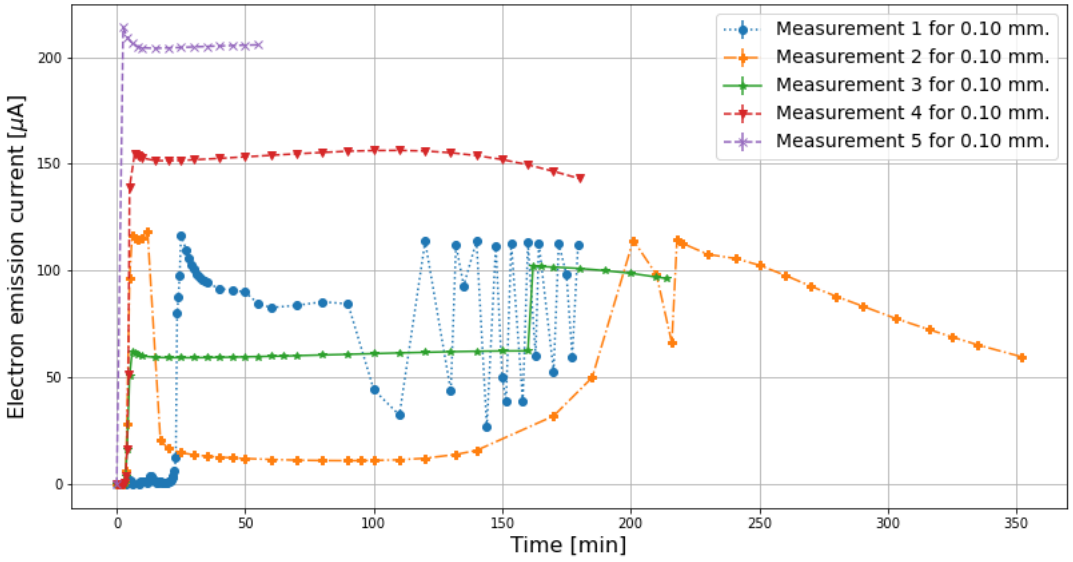

Figure 2.6: Measurements 1, 2, 3, 4, and 5 for the filament with a diameter of 0.10 mm showing the electron emission current as a function of time.

slightly higher than measurement 3 and therefore in the usual range for a conventional ion source system. Furthermore, even though the electron emission was not perfectly stable, the curve was still smooth, since no sudden burst nor any fast oscillation occurred. The mean electron emission over the last 160 minutes was 152.92 μA with a standard deviation $\sigma = 3.16$ μA. Moreover, the maximal variation between the two most different values was below 9.3 % over 160 minutes. Consequently, the electron emission stability would have been satisfactory for an optimisation session with a mass spectrometer.

Measurement 5 is shown in Figure 2.6. The cathode voltage was raised to 5.26 V, causing the cathode current to reach 1.18 A with 6.2 W and an electron emission of (204.99 ± 0.05) μA after 8 minutes. This emission was even stronger than previous measurements and reached the usual range of (100 to 1000) μA, even though the power used was much lower than previous measurements for a larger filament diameter of 0.15 mm that needed over 16 W (see e.g. measurements 5 in Figure 2.5 and 6 Figure 2.5). The mean electron emission over the last 47 minutes was 204.90 μA with a standard deviation $\sigma = 0.55$ μA. Furthermore, the maximal variation between the two most different values was below 0.9 % over 47 minutes, which was highly satisfactory, at least for a short measurement with a mass spectrometer. Since measurements 4 and 5 were carried out on the same day, the time with the cathode off in between was not long enough to cool the LEIS back down to room temperature, so the temperature started slightly below (67.8 ± 0.1) °C and ended up at (114.1 ± 0.1) °C. Therefore, the LEIS was used in the conditions of measurement 5 during less than an hour, which was too short to confirm whether the obtained high stability could be sustained over a full optimisation session of a few hours with a mass spectrometer.

After measurement 5 it was decided to continue with the ion box and the exit grid electrodes as in a previous version of the LEIS system before the tests with the acceleration rings described in Section 2.2.2. Furthermore, the temperature sensor was placed back outside, on the housing of LEIS on the side of the filament. This final configuration is described in Section 1.7 and was kept for the

rest of the filament testing and further use of LEIS. However, measurements 6, 7, and 8, namely the first measurements with this final configuration, were still carried out without gas in the vacuum chamber. The pressure in the vacuum chamber was (2 to 4) $\cdot 10^{-8}$ mbar.

Measurement 6 is shown in Figure 2.7. The cathode voltage was set to 5.14 V with a current of 1.16 A and a power of approximately 6 W. Thus, the electron emission current increased from (154.0 ± 0.05) μA to (190.0 ± 0.05) μA in 92 minutes. Then, the electron emission dropped to (40.66 ± 0.05) μA in only 30 minutes. Even though the curve was smooth, the electron emission was not stable enough for a use with a mass spectrometer.

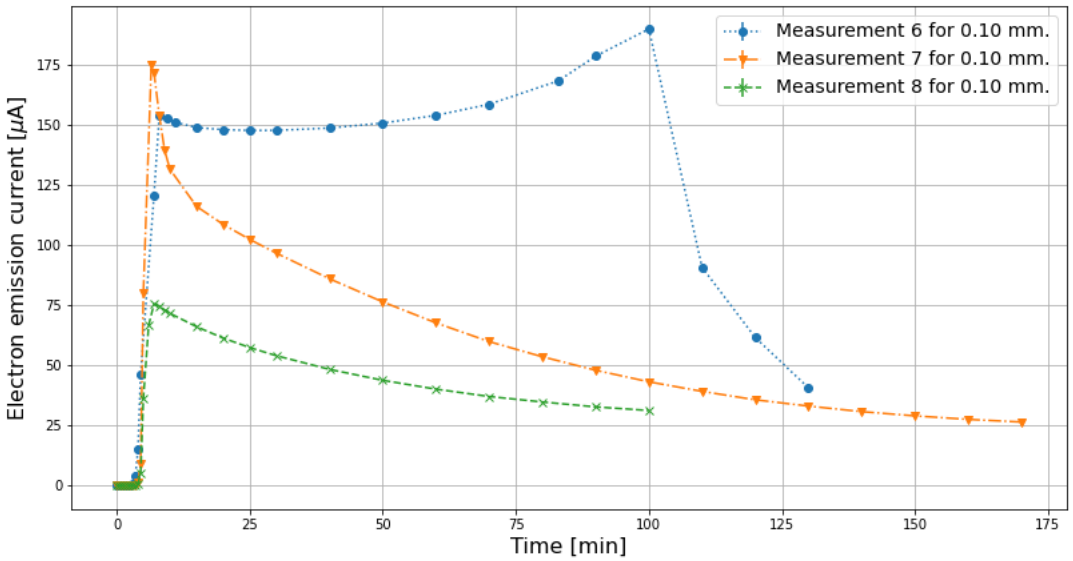

Figure 2.7: Measurements 6, 7, and 8 for the filament with a diameter of 0.10 mm showing the electron emission current as a function of time.

Measurements 7 and 8 both had a cathode voltage of 5.07 V and used about (5.85 ± 0.1) W. Both measurements are displayed in Figure 2.7. Measurement 7 started with a peak electron emission of (175 ± 0.05) μA, while that quantity was (75.55 ± 0.05) μA for measurement 8. No sudden burst or oscillation occurred. However, the electron emission current decreased towards (26.46 ± 0.05) μA for measurement 7 at 170 min and $(31.26 \pm 0.05$ $)\mu$A for measurement 8 at 100 min. Thus, the electron emission was neither high, nor stable enough for a measurement with a mass spectrometer. Furthermore, the ion box and the ion box exit grid could not be set to different potentials during all three measurements 6, 7, and 8, because of a wrong contact between both electrodes.

After the inspection of LEIS and its short repair, different potentials could be independently applied again to both electrodes. Thus, LEIS was used with gas for the first time with the 0.10 mm filament. Measurements 9, 10, and 12 were carried out with argon, whereas during measurements 11 and 13 no gas was added in the vacuum chamber staying at a pressure of about (2.41 to 4.74) $\cdot 10^{-8}$ mbar.

For measurements 9, 10, and 11, the LEIS cathode was set to 5.07 V, yielding a cathode current of 1.154 A with a consumed power of 5.85 W. Theses values are the same as for measurements 7 and 8. Furthermore, for measurements 9, 10, and 12, the pressure of argon was low and not strongly controlled, i.e. without manual adaptation of the gas inlet rate. Measurement 9 is shown in Figure 2.8. The pressure in the vacuum chamber without gas was $P_0 = (5.1 \pm 0.1) \cdot 10^{-8}$ mbar, while the pres-

sure with argon slowly decreased throughout the measurement from $P_{Ar} = (9.5 \pm 0.1) \cdot 10^{-8}$ mbar to $(5.69 \pm 0.1) \cdot 10^{-8}$ mbar. The last part of the electron emission seemed slightly more stable than the beginning. However, the emission decreased from (105.0±0.05) μA at 30 min to (76.55±0.05) μA at 80 min, even with a lowest value of (69.84±0.05) μA at 70 min. Therefore, the electron emission, whose mean value was 86.55 μA with a standard deviation of $\sigma = 9.20$ μA over the last 50 minutes, was not stable enough, even for a short measurement with a mass spectrometer.

After the same ramp-up as for measurement 9, measurement 10 also had a similar behaviour during the first 30 minutes with a high electron emission reaching (240.20±0.05) μA before decreasing to lower values, as it is shown in Figure 2.8. The pressure in the vacuum chamber without gas was $P_0 = (2.51 \pm 0.1) \cdot 10^{-8}$ mbar, while the pressure with argon slowly decreased throughout the measurement from $P_{Ar} = (9.30 \pm 0.1) \cdot 10^{-8}$ mbar to $(8.69 \pm 0.1) \cdot 10^{-8}$ mbar. The last part of the electron emission seemed slightly more stable than the beginning, since the curve was smooth. However, the emission decreased from (107.96±0.05) μA at 30 min to (48.44±0.05) μA at 130 min, which represented an even slightly stronger decrease rate than measurement 9. Therefore, the electron emission, whose mean value was 73.22 μA with a standard deviation $\sigma = 20.05$ μA over the last 100 minutes, was not stable enough, even for a short measurement with a mass spectrometer.

Measurement 11 was carried out without gas in the vacuum chamber with and is displayed in Figure2.8. The pressure in the chamber was $(2.41 \pm 0.1) \cdot 10^{-8}$ mbar. After reaching a maximal electron emission of (161.18 ± 0.05) μA at 16 min, the emission current smoothly decreased to (90.74±0.05) μA at 80 min. Thus, under the same cathode voltage and current as for measurement 9 and 10, measurement 11 reached a lower maximal electron emission and the decrease after that value was smoother, without any drastic peak-like shape. However, the mean electron emission was 120.16 μA with a standard deviation $\sigma = 24.14$ μA over the last 54 minutes, which meant an even larger average decrease rate than both measurements 9 and 10.

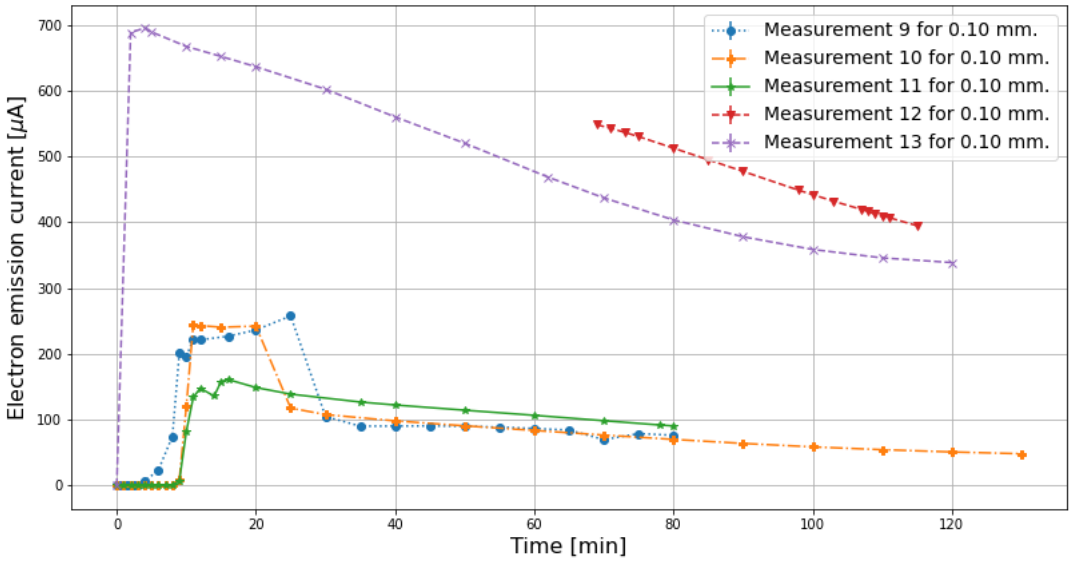

Figure 2.8: Measurements 9, 10, 11, 12, and 13 for the filament with a diameter of 0.10 mm showing the electron emission current as a function of time.

The filament was ramped up for measurement 12 with +0.5 V per minute until 5.0 V were

reached. As can be seen in Figure 2.8, the first part of the measurement is less relevant to the investigation of stability, since the cathode voltage was slightly raised five times until 42 min and argon was brought inside the vacuum chamber at 36 min and, finally, the gas concentration was increased again at 54 min. The pressure in the vacuum chamber without gas was $P_0 = (2.43 \pm 0.1) \cdot 10^{-8}$ mbar, while the pressure with argon slowly decreased throughout the measurement from $(5.77 \pm 0.1) \cdot 10^{-7}$ to $(4.86 \pm 0.1) \cdot 10^{-7}$ mbar. The filament voltage at 69 min was 5.75 V and was kept constant from that time point on, with its current of 1.24 A for an approximate power of 7.13 W. The electron emission current, was (548.0 ± 0.1) μA at 69 min and smoothly decreased to (394.8 ± 0.1) μA at 115 min. Therefore, the electron emission, whose mean value was 463.96 μA with a standard deviation $\sigma = 55.47$ μA over the last 46 minutes, was not stable enough, even for a short measurement with a mass spectrometer. However, the electron emission decrease rate was constant enough to make the curve look linear, since its mean value was -3.23 μA/min with a standard deviation $\sigma = 0.49$ μA/min.

—-»» Compare this emission with a previous value 400-600 uA with regards to power used!

Measurement 13, shown in Figure 2.8, was carried out without gas in the vacuum chamber and the pressure was $P_0 = (2.60 \pm 0.1) \cdot 10^{-8}$ mbar for $T = (41.7 \pm 0.1)$ °C at the beginning of the measurement. The filament voltage was 5.75 V for measurement 13 with a cathode current of 1.245 A at 2 min with an approximate power of 7.16 W). The electron emission current reached (688.0 ± 0.1) μA at 2 min and smoothly decreased to (338.8 ± 0.1) μA at 120 min. Therefore, the electron emission, whose mean value was 527.47 μA with a standard deviation $\sigma = 136.56$ μA over 118 minutes, was not stable enough, even for a short measurement with a mass spectrometer, even though the curve was smooth and displayed no burst, no oscillation, no sudden change.

After measurement 13, there was a power outage of about two hours in Bern on a Sunday. Thus, during that short time, the quality of the vacuum could not be guaranteed. So, after being left under a controlled vacuum for more than a day, the filament was conditioned again as if it had been air-exposed. Therefore, the goal of measurement 14 was to keep a high emission current (around 500 to 600 μA) for as long as the rising temperature would allow, as an attempt to clean the wire surface from possible gas contamination, not to keep the same filament voltage for stability investigation. Measurements 14, 15, and 16 were all carried out within a few days after the power outage.

Measurement 14 was carried out without gas in the vacuum chamber with a pressure of $P_0 = (3.31 \pm 0.1) \cdot 10^{-8}$ mbar for $T = (25.0 \pm 0.1)$ °C at the beginning of the measurement and the result is depicted in Figure 2.9. After a first continuous increase of the filament voltage, 5.5 V were reached in 2 min for an approximate power of 6.66 W. Then, the voltage was increased to 5.7 V at 9 min and 5.8 V at 62 min. After each of these voltage settings the electron emission smoothly decreased. Finally, the wire voltage was set to 5.9 V with a current of 1.258 A and a power of $\sim$ 7.42 W, yielding to an initial electron emission current of 616 μA at 116 min. The electron emission first started to decrease, before increasing again, while always staying on a smooth curve. The final electron emission current reached 649 μA at 230 min. Moreover, the mean electron emission current was 598.0 μA with a standard deviation $\sigma = 25.72$ μA over the last 114 minutes. Consequently, the electron emission was not stable enough for a $2-4$ h optimisation session with a mass spectrometer, but could be used for a shorter measurement. Furthermore, for a given voltage applied to the filament the curve was smooth and an emission around 500 to 650 μA could be manually maintained over almost 4 hours.

Measurement 15, which is illustrated in Figure 2.9, started with no gas in the vacuum chamber, since the pressure was $P_0 = (3.30 \pm 0.1) \cdot 10^{-8}$ mbar for $T = (23.1 \pm 0.1)$ °C. After a short ramp-up time of 2 min, a cathode voltage of 5.75 V was reached with a current of 1.245 A with an approximate power of 7.16 W), yielding an electron emission current of (820.0 ± 0.1) μA. The beginning of the electron emission decrease was strong, but the average slope was less steep from 10 to 140 min, when

the emission decreased from (695.0 ± 0.1) μA to 498.0 ± 0.1 μA, which represented a mean decrease rate of -1.56 μA/min with a standard deviation of 0.47 μA/min. At 142 min the filament voltage was slightly raised to 5.80 V with a current of 1.245 A and an approximate power of 7.22 W). Thus, the mean electron emission current was 536.43 μA with a standard deviation $\sigma = 11.60$ μA during the next 58 min. Furthermore, the maximal difference between the two extreme values during that period was below 5.6 %, which could point towards satisfactory stability for short measurements below an hour with a mass spectrometer for an electron emission current above 500 μA. However, it should be noted that this stability was observed without gas. At 203 min, argon was let in inside the vacuum chamber and made the pressure rise to $(8.14 \pm 0.05) \cdot 10^{-7}$mbar at 81.3°C. The electron emission slightly increased from (455.0 ± 0.1) μA to (488.0 ± 0.1) μA in 32 min, namely 7.3%, but the end of the measurement was too early to conclude about stability. As a conclusion, it is worth mentioning that the electron emission reached levels in the higher part of the usual range of (100 to 1000) μA with a final temperature on the LEIS housing of only 84.1°C, which demonstrated the possibility to continuously use the LEIS during almost 4 h without damage.

Measurement 16, shown in Figure 2.9, started with similar settings as measurement 15: no gas in the vacuum chamber with $P_0 = (3.18 \pm 0.1) \cdot 10^{-8}$ mbar for $T = (23.2 \pm 0.1)$ °C, a short ramp-up time of 2 min, a cathode voltage of 5.75 V with a current of 1.247 A going down to 1.240 A after 10 min, and a approximate power of 7.17 W, leading to a starting electron emission current of (753.0 ± 0.1) μA. The emission quickly fell down to (668.0 ± 0.1) μA at 10 min, before decreasing with a less steep slope, similarly to measurement 15. Thus, the electron emission reached (622.0 ± 0.1) μA at 80 min, which represented a mean decrease rate of -0.65 μA/min with a standard deviation of $\sigma = 0.2$ μA/min. Thus, the decrease rate in the first part was stronger in measurement 15 than in measurement 16. Then, after 80 min, argon was let in inside the vacuum chamber whose pressure became $P_{Ar} = (8.40 \pm 0.05) \cdot 10^{-7}$ mbar for $T = (56.3 \pm 0.1)$ °C. Under the exact same filament power conditions, the electron emission slightly shifted to a lower level, going from (622.0 ± 0.1) μA to (553.0 ± 0.1) μA because of the presence of argon. During that last part of the measurement the mean electron emission decrease rate was -0.69 μA/min with a standard deviation $\sigma = 0.33$ μA/min, which was similar to the first part without gas. Moreover, during the last 75 min the maximal variation represented 10.2 %. Consequently, the electron emission stability might have been slightly too low for a 75-minute measurement with a mass spectrometer, even though measurements of a few minutes would have been acceptable. However, a smooth electron emission could be maintained above 500 μA over 160 min with a reasonable final temperature on the LEIS housing of $T = (76.2 \pm 0.1)$ °C.

Measurement 17, which is depicted in Figure 2.9, was carried out without gas in the vacuum chamber, since the pressure was $P_0 = (3.85 \pm 0.05) \cdot 10^{-8}$ mbar for $T = (22.8 \pm 0.1)$ °C.This measurement was taken three weeks after measurement 16, i.e. after a run time of the cathode > 690 min for other measurements which are not displayed here. After a short ramp-up time of 2.5 min during which the cathode voltage was continuously increased to 5.0 V with an approximate power of 5.76 W), before being set to 5.5 V with an approximate power of 6.66 W at 6.5 min, yielding an electron emission current of (445.0 ± 0.1) μA. The electron emission quickly decreased to (319.0 ± 0.1) μA at 15 min, thus showing a cathode stabilisation time of at least about 10 to 20 min. The decrease continued down to (289.0 ± 0.1) μA at 70 min, but with a much flatter slope, since the mean electron emission was 302.33 μA with a standard deviation of 9.31 μA. At 72 min, the voltage was set to 5.6 V with an approximate power of 6.84 W leading to an electron emission of (367.0 ± 0.1) μA. Then, at 82 min, the voltage was lowered down to 5.55 V with an approximate power of 6.74 W to reach an electron emission of (325.0 ± 0.1) μA. Furthermore, after 82 min, and thus during the last 48 min, the mean electron emission was 319.73 μA with a standard deviation $\sigma = 3.77$ μA and the maximal deviation between the two most different values was below 3.6 %,

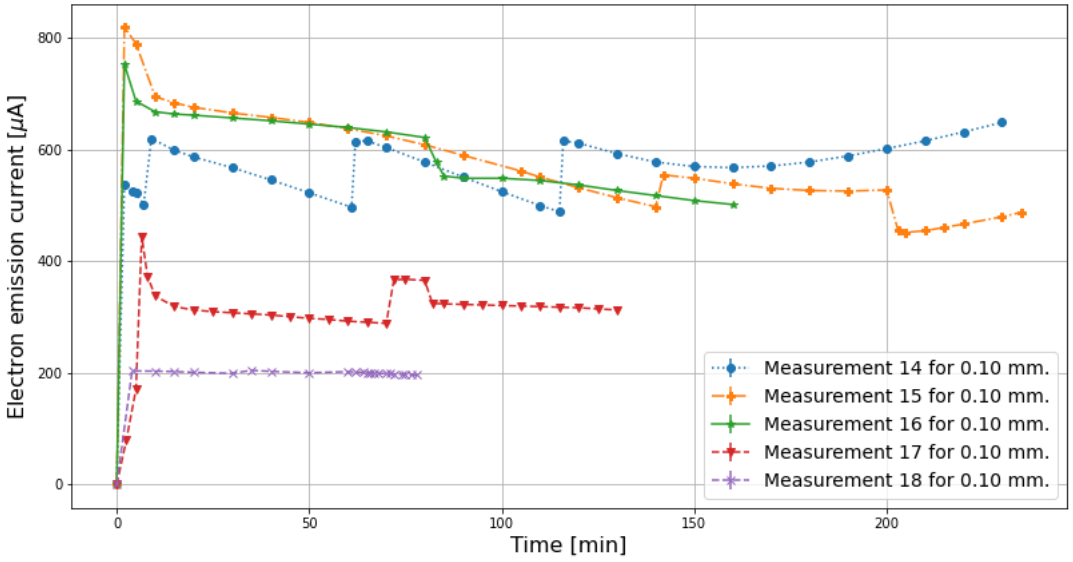

Figure 2.9: Measurements 14, 15, 16, 17, and 18 for the filament with a diameter of 0.10 mm showing the electron emission current as a function of time.

which demonstrated a high stability. As a consequence, the electron emission was similar to the values used for the NIM instrument (Föhn et al., 2021) and in the usual range of (100 to 1000) μA and was highly stable during more than 45 min, which might have been enough for at least a short measurement with a mass spectrometer.

Finally, measurement 18, the last presented here and displayed in Figure 2.9, was carried out seven weeks after measurement 17, which means that the LEIS filament had been used for more than 30 h between both measurements. The pressure inside the vacuum chamber before the beginning of the measurement was $P_0 = (2.18 \pm 0.1) \cdot 10^{-8}$ mbar for $T = (22.7 \pm 0.1)$ °C. Then, argon was let in before the cathode ramp-up to increase the pressure in the vacuum chamber to $P_{Ar} = (3.54 \pm 0.05) \cdot 10^{-7}$ mbar for $T = (46.0 \pm 0.1)$ °C. The goal of this measurement was to aim for an electron emission of 200 μA, while correcting the filament voltage when needed. The voltage ramp-up was about 0.1 V/s and the cathode voltage was first set to 5.22 V with an approximate power of 6.13 W. Thus, during the first phase of the measurement, the mean electron emission was 202.12 μA with a standard deviation σ of 1.77 μA. A first adaptation was needed at 35 min, so the cathode voltage was set to 5.23 V with an approximate power of 6.14 W. Finally, one last voltage modification was needed at 60 min with 5.24 V and with an approximate power of 6.16 W. Throughout the full measurement, the overall mean electron emission was 200.42 μA with a standard deviation $\sigma = 2.34$ μA.

Therefore, this measurement shows that an emission current of 200 μA with a mean argon pressure of $3.52 \cdot 10^{-7}$ mbar with a standard deviation $\sigma = 0.03 \cdot 10^{-7}$ mbar can be maintained to a stable level if 1 to 2 filament voltage adaptations are allowed per hour, which means that the LEIS can be used for long optimisation sessions with mass spectrometers. Consequently, it is not unreasonable to expect the LEIS to correctly work for mass spectrometry with a wider range of electron emission currents and other gases, provided that the operator keeps track of the electron emission and slightly adapts the filament voltage when needed.

2.2.6 Discussion of the Emission Stability for 0.10 mm

Thanks to all tests conducted on wire candidates for LEIS, a convenient tungsten filament has been found with an approximate length of 50 mm and a diameter of (0.10 ± 0.01) mm. A thicker wire usually means a longer lifetime, but also a higher consumed power. Since LEIS is a ground testing device and it does not need to fly to space, occasionally changing the emission wire is a suitable trade-off. Furthermore, as of August 2025, the same thin filament had been in use within LEIS for a year and it was still correctly working.

The filament tests indicated that a brand new wire usually needs to be used during several sessions of a few hours each after bake-out. Then, each time the filament is air-exposed, a few sessions are needed to reach a satisfactory stability again. Finally, the tendency seemed to show that the more it had been used, the lower the number of repetitions before satisfactory stability needed to be.

Electron emission currents above 600 μA and a continuous use of the cathode during several hours were achieved in a vacuum chamber without cryopumps. It is thus worth noticing that the temperature increase rate being the main limiting factor on time, cryopumps contribute to an improvement for the time of continuous use of the wire. Moreover, sporadic corrections of the filament voltage by the operator enable a longer period during which the electron emission current is maintained at a stable level. Consequently, LEIS in its current version with its filament diameter of 0.10 mm can be a handy ion source for testing and optimisation sessions of over 2 to 4 h with a mass spectrometer.

Chapter 3

Thermal and Ion Measurements with OpenTOF

3.1 Measurement in Thermal Mode for Argon

Parameter	**Value**
Q-BP_Pulser	600 V
Q-AccL	-1229 V
Q-D_Pulser	-3000 V
Drift	-3000 V
D-L	-1351 V
R-L0	-4014 V
VD-R_B	399 V
R-BP	568 V
MCP-F	-3000 V
Anode	-950 V
Q-Gr	1.80 V
$I_{Filament}$	145 μA

Table 3.1: Settings for the spectrum measurement of argon in thermal mode with OpenTOF as a first check after the installation of the LEIS in the chamber. Most of the values are taken from Iseli (2024), except $I_{Filament}$ and $Q - Gr$. The voltage over the MCP stack was + 2050 V for the actual measurement and + 1800 V for the background measurement. Should we not mention MCP-F in the table?

The first use of OpenTOF after the LEIS was included in the chamber was successful in pointing that OpenTOF was still working properly. This first spectrum measurement of argon in thermal mode was carried out with a pressure in the chamber of about $3.67 \cdot 10^{-7}$ $mbar$ and with the settings described in Table 3.1. The measurement showed one high peak at $4.89 \mu s$ (9781 arbitrary units) and one lower at $3.51 \mu s$ (7012 arbitrary units). Since the pressure in the chamber was $3.20 \cdot 10^{-9}$ $mbar$ before argon was let in, it is safe to assume that the main peak at 3.51 μs is due to argon that had been one time ionised, as argon was the main component in the chamber. The energy carried by the ionising electrons is of the order of magnitude of 70 eV. Thus, the energy is too low to break the

argon atom in a smaller fragment. There might be two first hypotheses to explain the presence of a secondary peak at 4.89 μs: either rest gas from the venting in the chamber or from the gas inlet due to a previous use. The relative area of the secondary peak is slightly less than 7% of that of the main one. Furthermore, the pressure in the gas chamber before the measurement ($3.20 \cdot 10^{-9}$ $mbar$) was about 100 times lower than when argon was let in ($3.67 \cdot 10^{-7}$ $mbar$). As a consequence, it is highly unlikely that rest gas from venting, left in such low quantities, would yield such a high relative intensity. Between each refill of the gas inlet reservoir or after a bottle change, the gas inlet on the chamber and the bottle are both closed and the reservoir content is pumped away by a small pump. This process is repeated at least twice when the bottle is changed to get rid of unwanted gases (e.g. N_2, O_2, H_2O from air). If the pumping is not efficient enough tiny traces of other gases might have stayed in the reservoir. However, the same argon bottle had been previously used without being unmounted from the reservoir. Therefore, contamination of the gas reservoir during the setup changes in the chamber being excluded, rest gas as the reason for a secondary peak is discarded. The third option is much likely to be the correct answer: some argon atoms were ionised twice by the ionisation filament and needed thus a much shorter time of flight to pass through the instrument.

3.2 Measurement in Thermal Mode for FC5311

A spectrum of FC5311 was measured in thermal mode without the delay-pulser. Therefore, the voltage on the delay-pulser electrode *Q-D-Pluser?* had to be set to the same value as the drift tube. Table 3.2 shows initial values computed thanks to simulations by Schertenleib (2023), experimental values found by Iseli (2024), and settings used for this work. For the sake of visual clarity, the voltages for the measurement carried out by the author are rounded in Table 3.2 to the closest volt value, except for the ground voltage of the source *Q-Gr*. Thus, one might take an uncertainty on the settings of 0.5 V. Generally, a tension difference of about 1 V on all voltage but *Q-Gr* had little effect on the spectrum displayed on screen thanks to the acquisition software, while a few tenths of a volt on *Q-Gr* were enough to significantly change the shape and height of peaks.

Parameter	**Simulations [V]** Schertenleib (2023)	**Previous Work [V]** Iseli (2024)	**This Work [V]**
Q-BP_Pulser	600	600	600
Q-Gr	0	3.65	2.40
Q-AccL	-1650	-1229	-1231
Q-D_Pulser	-3000	-3000	-3001
Drift	-3000	-3000	-3002
D-L	-1420	-1351	-1352
R-L0	-3485	-4014	-4016
VD-R_B	465	399	398
R-BP	605	568	566
MCP-F	-3000	-3000	-3000

Table 3.2: Settings for the spectrum measurement of FC5311 in thermal mode with OpenTOF.

3.2.1 Method for Argon Ion Detection with OpenTOF at 10 km/s

After the LEIS was dismounted from its previous vacuum chamber with the Faraday cup and mounted in the same vacuum chamber as OpenTOF, the MCPs were conditioned, and the tungsten wire of LEIS was also prepared according to the guidelines described in Section 5. Then, a spectrum measurement of argon was carried out with OpenTOF using its ionisation filament and the optimised settings of the thermal mode (according to previous work byIseli (2024)). The LEIS was not switched on during this measurement, since its goal was to check that OpenTOF was still working properly after the latest changes in the vacuum chamber.

3.3 Ion Peak Area as a Function of Electron Emission for 10 km/s

When an ion impacts OpenTOF's detector, a high number of electrons are generated by the MCPs, thus producing a current on the detector's circuit. The number of generated electrons can be compared between two measurements, provided the quality of the MCPs or the voltage over the stack have not changed and the gain is kept constant. Since the resistance of 50 Ω is a constant, the voltage measured by the acquisition board is proportional to the current. The data of the mass spectrum measurement shows a voltage as a function of time of flight. Therefore, The current as a function of time is known and the areas under the curve can be computed to yield a charge in coulombs that could also be converted to a number of counts, since the elementary charge e is also known. Consequently, the peak areas in a mass spectrum are directly proportional to the initial number of ions impacting the detector.

At a given gas pressure, and for a given sets of voltages used for ion acceleration, if the electron emission current of LEIS is increased, the ion flux generated is increased. To study the effects on the mass spectra, OpenTOF was used to measure the peak area of argon as a function of the LEIS electron emission, which was varied between 0 and slightly above 5000 μA. LEIS was placed along OpenTOF's aperture axis at a distance of 10 mm, as is also depicted in Figure2.2. Since the instrument was targeted with fast ions instead of fast gas, OpenTOF's ionisation filament was turned off during the measurements. This section presents the results for argon at 10 km/s, which were similar to those for 20 km/s.

The mass spectrum acquisition software was set to accumulate $10,000$ spectra and sum them at a frequency of $10,000$ Hz, the period between two pulses on the extraction pulser being 100 μs, thus creating one full mass spectrum per second. Each spectrum was then saved into its own folder. First, the raw data generated by the acquisition board was translated into workable data by a custom code written in Python. This transformed data displays a voltage measured on the detector as a function of the time. Then, all spectra could be summed, thus yielding a fully accumulated mass spectrum with a higher signal-to-noise ratio. For this measurement 60, mass spectra were measured, thus representing 60 seconds. The settings of LEIS and OpenTOF are summarised in Table 3.3. After the voltage curve was converted into a current thanks to a division by the resistance of 50 Ω, the data could be integrated. The area under the peaks therefore represent the accumulated charges over the full accumulation time of 60 s. These accumulated charges were divided by 60 s to yield an average current measured on the detector. The process was repeated for several LEIS emission currents and plotted in Figure 3.1. The exact value of a peak area depends on the way the edges of the peaks are identified when the baseline is not a flat line. It was chosen to keep a conservative approach in this work by computing for each peak the smallest possible area and the largest. Then, the average was taken as the final area, with the difference to the extreme values being the uncertainty on the area.

Figure 3.1 shows that the peak area increased with higher LEIS electron emission, which is expec-

Parameter LEIS for Ar^+ at 10 km/s	**Value**	**Parameter** OpenTOF for 10 km/s	**Value**
Cathode bias	-49.3 V	Q-BP_Pulser	600 V
Extraction	180.7 V	Q-AccL	-2300 V
Ion box	21.7 V	Q-D_Pulser	-5000 V
Ion box exit grid	19.7 V	Drift	-5000 V
Electron collector grid	60.0 V	D-L	-2200 V
Electron collector	100.0 V	R-L0	-6000 V
Backplane and housing	GND = 0 V	VD-R_B	640 V
Electron emission	0 to 5000 μA	R-BP	1080 V
		MCP-F	-5000 V
		Anode	-2900 V
		Q-Gr	-2.0 V
		$I_{Filament}$	0 μA

Table 3.3: Settings for the spectrum measurement of argon ions at 10 km/s with OpenTOF and LEIS.

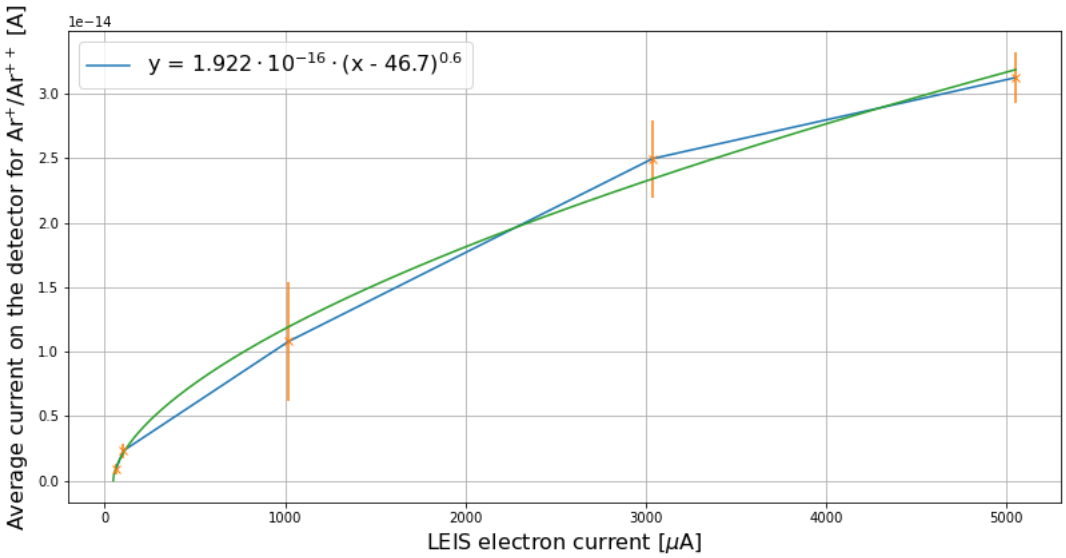

Figure 3.1: Argon peak area as a function of the LEIS electron emission. The peak area accounts mainly for Ar^+, but also for small amounts of Ar^{++}. The pressure in the vacuum chamber had a mean value of $3.66 \cdot 10^{-7}$ mbar with a standard deviation of $0.12 \cdot 10^{-7}$ mbar and the ion speed was 10 km/s. The voltage over the MCP stack was +2100 V.

ted since a higher ion density at a given velocity yields a higher count on the detector. Furthermore, the higher the electron emission, the lower the positive slope. This effect was also observed with the ion yield of LEIS. Thus, a function of the following form was used to fit the data:

$$y = a \cdot (x - b)^c. \tag{3.1}$$

A set of tens of initial seeds were used with the function *curve_fit*, taken from the Python module *scipy.optimize*. Since all results were close, the average was computed and taken as the final values for the three parameters. The final fitting function was for x, the electron emission in μA, and y, the average current on the detector in A:

$$y = 1.922 \cdot 10^{-16} \cdot (x - 46.7)^{0.6}. \tag{3.2}$$

This measurement is a first proof of concept, showing that the instrument works with ions at 10 km/s. Furthermore, an unambiguous peak detection was demonstrated for electron emission as low as 63 μA. Possible future improvements may include an increased focus on the ion beam of LEIS, e.g. using acceleration rings, and a detector with a slightly higher performance.

With the same method as described in this section clear detections of Ar^+ and Ar^{++} at 20 km/s were achieved as clearly as for Kr^+ at speeds between 10 km/s and 15 km/s. Finally, pushing the previous conservative limits of 200 V on LEIS, an energy of 250 eV was used with Xenon, thus achieving a detection at a high speed of 19 km/s.

Chapter 4

Measurements with LEIS, OpenTOF, and the Conversion Surface

The final version of the setup with LEIS had the ability to generate fast gas alongside fast ions. LEIS was attached to a conversion surface, or neutraliser, as explained in Chapter 1. The distance between the edge of the conversion surface and OpenTOF's aperture was (20 ± 1) mm. This chapter explains the measurements carried out to detect ionised gas and neutralised ions with OpenTOF at high relative velocities up to 17 km/s.

4.1 Measurements with Xenon at 17 km/s

Measurement 1 was carried out with xenon and a pressure of $(3.44 \pm 0.1) \cdot 10^{-7}$ mbar in the vacuum chamber. The targeted speed was 17 km/s, the accumulation time for each measurement was 120 s, and the electron emission in LEIS was (5021 ± 30) μA, whereas the electron emission due to OpenTOF's filament was (198.5 ± 2.0) μA. The speed interval for all detected xenon isotopes was $[16.68, 17.37]$ km/s. The other settings are shown in Table 4.1. The attempts to detect neutrals with OpenTOF always followed the same procedure to gather 6 different data sets in similar conditions, but with one specific parameter changed. First, a measurement 1.a was taken with the LEIS cathode on, the OpenTOF ionisation filaments on too, and the pressure gauge of the vacuum chamber. This measurement yielded a total signal accounting for a thermal, an ion, and a neutral contribution. The pressure gauge releases electrons. Even though electrons from the gauge were not supposed to interact much with the instrument, due to the position at the back of the vacuum chamber, a second similar measurement was taken with the pressure gauge off, as a verification. That new measurement 1.b was carried out in conditions as close to 1.a as possible, but without the gauge. A significant difference between signals 1.a and 1.b was not detected during the data processing. However, as a safety precaution, the pressure gauge was left switched off until the end of the series of measurements. Then, measurement 1.c was taken with the LEIS cathode on, but the OpenTOF filament off, thus yielding the ion signal. The next measurement, 1.d, had the inverse settings, so the LEIS cathode off, but the OpenTOF filament on to measure only the thermal signal. Finally, two background measurements were carried out: one with the same MCP voltage, but both filaments off, labelled 1.e and another, 1.f, with both filaments on, but the voltage over the stack at +1500 V instead of +2100 V. The result of this measurement series 1 is shown in Figure 4.1.

Four different curves belonging to measurement series 1 are displayed in Figure 4.1, in which the cumulated voltage on the detector over 120 s is plotted as a function of the time of flight. The blue curve stands for the purely thermal signal 1.d. As expected, the thermal signal yielded the highest

Parameter LEIS for Xe^+ at 17 km/s	**Value**	**Parameter** OpenTOF for 17 km/s	**Value**
Cathode bias	120.0 V	Q-BP_Pulser	600 V
Extraction	160.0 V	Q-AccL	-1831 V
Ion box	200.0 V	Q-D_Pulser	-5000 V
Ion box exit grid	196.0 V	Drift	-5000 V
Electron collector grid	97.5 V	D-L	-1319 V
Electron collector	249.5 V	R-L0	-6000 V
Backplane and housing	GND = 0 V	VD-R_B	931 V
Electron emission	(5021 ± 30) μA	R-BP	1120 V
		MCP-F	-5000 V
		Anode	-2900 V
		Q-Gr	0.0 V
		$I_{Filament}$	(198.5 ± 2.0) μA

Table 4.1: Settings for the spectrum measurement of xenon at 17 km/s using OpenTOF and LEIS with its neutraliser.

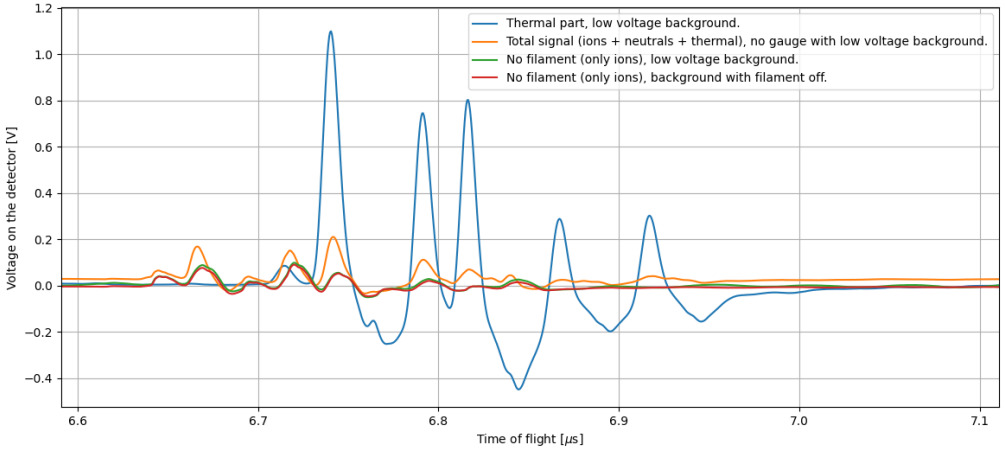

Figure 4.1: Measurement series 1. Cumulated voltage over 120 s on the detector as a function of the time of flight. The pressure in the vacuum chamber filled with xenon was $(3.44 \pm 0.1) \cdot 10^{-7}$ mbar and the speed of xenon was 17 km/s. The voltage over the MCP stack was +2100 V.

peaks, since the electron beam of OpenTOF creates a negative potential well that stores low-energy ions between two extraction pulses. Since the order of magnitude for such a well is below 2 V, fast singly-charged ions and fast gas with an energy around 198 eV do not benefit from this ion storage effect. The orange curve represents the total signal 1.b. Finally, the green and the red curves both show the ion signal 1.c, but using different background measurements. Both signals were close, but the red curve using the background without filament yielded a flatter baseline, so this curve was kept for the next computations.

The first striking observation was that the total signal overlapping the purely thermal signal had shorter peaks, even though the thermal signal was supposed to be only one contribution to the full

sum of ions, neutrals, and the thermal part. The first hypothesis to explain this effect is to consider that a high ion flux might hinder the usual ion storage effect.

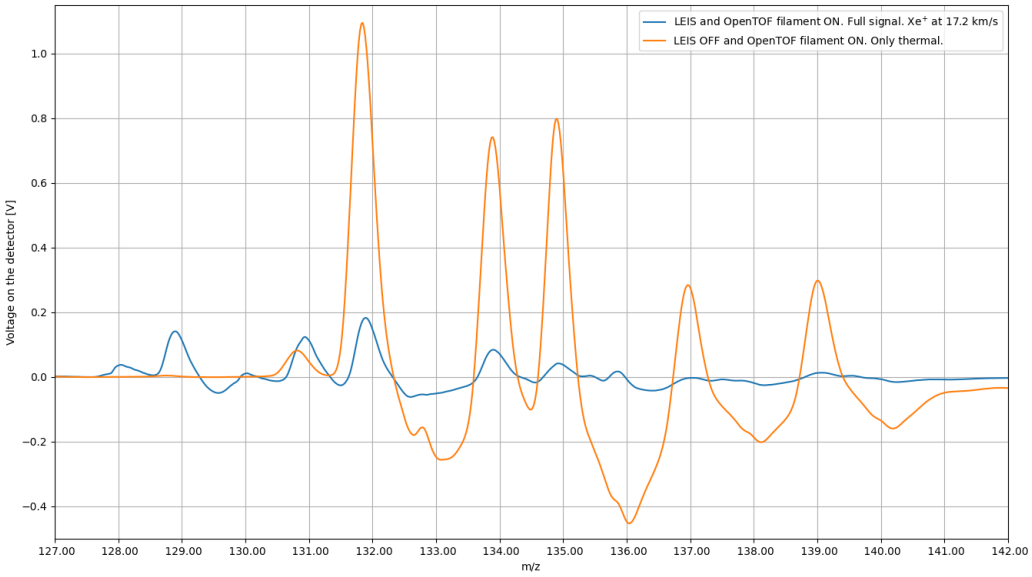

Figure 4.2: Mass-calibrated measurement series 1. Cumulated voltage over 120 s on the detector as a function of the time of flight. The pressure in the vacuum chamber filled with xenon was $(3.44 \pm 0.1) \cdot 10^{-7}$ mbar and the speed of xenon was 17 km/s. The voltage over the MCP stack was +2100 V. The full signal only was used for the mass calibration.

Figure 4.2 shows the same data as Figure 4.1, but only the thermal curve in orange and the total signal in blue for readability, after mass calibration using the total signal and baseline alignment. The thermal peaks are positioned close to masses 131, 132, 133, 134, 135, 137, and 139 instead of the correct masses of isotopes 128, 129, 130, 131, 132, 134, and 136 (Coursey et al., 2015). This is a proof of concept that the ion-optical system of OpenTOF works as expected. By design, the instrument separates the thermal signal from the fast gas to enable a distinction between long-lasting outgassing contributions and the fast gas from the investigated atmosphere. The mass shift was about 2.94, which is consistent with simulations of the instrument carried out by Schertenleib et al. (2024).

The same data as in Figure 4.2 was used with an independent mass calibration for each data set: one for the the total signal and another for the thermal curve. Thus, the thermal signal was automatically shifted to keep the same isotopes in both curves aligned. The result can be seen in Figure 4.3, in which the blue curve represents the full signal and the orange curve the thermal measurement. The blue curve also showed a peak at mass 135, whereas xenon does not possess an isotope 135 (Coursey et al., 2015), so no neutral or ion contribution is possible. Thus, this peak was entirely due to thermal xenon 132. For this specific peak, the area under both curves were computed to represent the particle counts. The ratio $Ratio_{th}$ between both areas accounts for the thermal change between both measurement modes. Under the practical assumption that this ratio was conserved for all peaks, this ratio was used to estimate the thermal contribution of peak 132 in the blue curve with the total signal. The abscissa was mass-calibrated for the sake of clarity to the reader, but the data was kept with a current on the detector as a function of the time of flight for

the area integration to correctly determine the total charge on the detector.

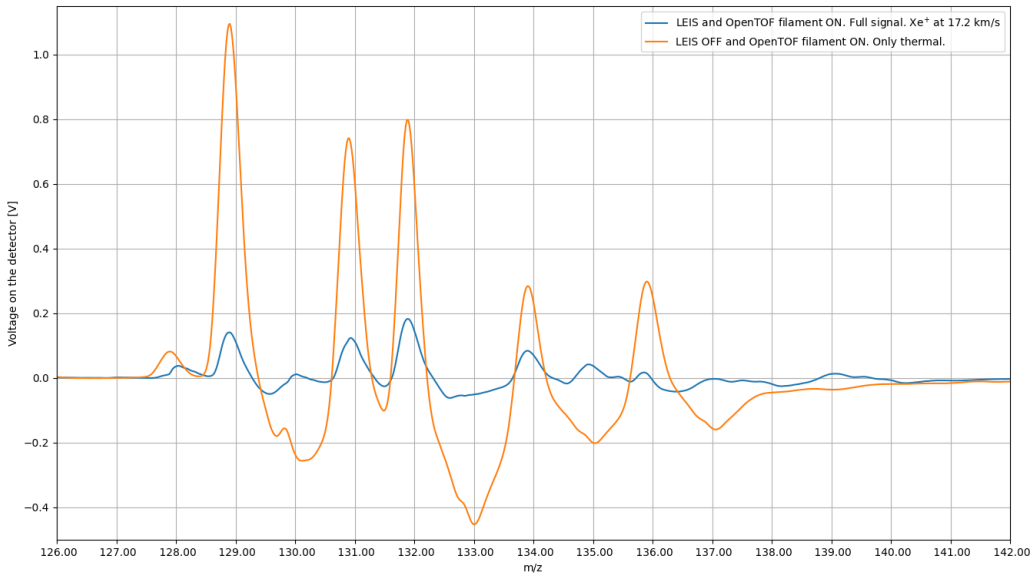

Figure 4.3: Independently mass-calibrated measurement series 1. Cumulated voltage over 120 s on the detector as a function of the time of flight. The pressure in the vacuum chamber filled with xenon was $(3.44 \pm 0.1) \cdot 10^{-7}$ mbar and the speed of xenon was 17 km/s. The voltage over the MCP stack was +2100 V. Both curves were independently mass-calibrated, hence the artificial peak alignment.

For the blue curve, let A_{tot135} be the area of the total peak at position $m/z = 135$ and A_{tot132} be the area of the total peak at $m = 132$. Furthermore, for the orange curve, let A_{th132} be the area of the thermal peak at position $m/z = 132$ and A_{th129} be the area of the thermal peak at $m = 129$. The change in thermal signal between a measurement with all contributions and a measurement in thermal mode only could be summarised by the ratio $Ratio_{th}$:

$$Ratio_{th} = \frac{A_{tot135}}{A_{th132}} \ . \tag{4.1}$$

Therefore, the thermal contribution $A_{thcontrib132}$ to the total peak area A_{tot132} at position $m/z = 132$ might be estimated as:

$$A_{thcontrib132} = Ratio_{th} \cdot A_{th129} \ . \tag{4.2}$$

The red curve in Figure 4.1 represents the ion signal alone. Moreover, let A_{ion132} be the area of the ion peak at $m = 132$. Consequently, the contribution $A_{neutrals132}$ of fast neutrals in the total peak at position $m/z = 132$ may be expressed as:

$$A_{neutrals132} = A_{tot132} - A_{thcontrib132} - A_{ion132} \ . \tag{4.3}$$

This approach yielded the following estimated contributions to the total signal at $m = 132$:

$$\frac{A_{thcontrib132}}{A_{tot132}} \approx 3.1\ \% \quad \frac{A_{ion132}}{A_{tot132}} \approx 47.3\ \% \quad \frac{A_{neutrals132}}{A_{tot132}} \approx 49.6\ \% \ .$$

These results showed that neutral fast gas of mass $m = 132$ u was correctly detected by OpenTOF at a relative speed of about 17 km/s.

As can be observed in Figure 4.2 the total peak at position position $m/z = 129$ was not overlapped by any thermal peak of the blue curve, because of the foreseen time delay expressed as a mass shift. Thus, the only two possible contributions to this peak area are the fast ion signal and the fast neutral signal. Therefore, the fast neutral contribution $A_{neutrals129}$ may be simply determined:

$$A_{neutrals129} = A_{tot129} - A_{ion129} = 9.027 \cdot 10^{-12}\ C\ .$$

This is further evidence that neutral fast gas was detected at 17 km/s. However, the ratio of detected neutrals 129 to neutrals 132:

$$Ratio_{neutrals129to132} = \frac{A_{neutrals129}}{A_{neutrals132}} = 34.8\ \%\ .$$

Given the isotopic composition of xenon on Earth with percentages of 26.40 % and 26.91 % (Coursey et al., 2015), the expected value for $Ratio_{neutrals129to132}$ was rather 98.1 %. This discrepancy is due to the prototype nature of the current detector, providing a baseline with a strong undershoot of the signal after high peaks. As of August 2025, a new detector is currently being tested with highly satisfactory results and this detector will soon replace the previous version, yielding a robust and stable baseline. Therefore, this issue has already been addressed and will be totally solved for the soon to be released brand new version of OpenTOF.

The ratio of detected fast ions 129 to fast ions 132 may also be determined as:

$$Ratio_{ions129to132} = \frac{A_{ions129}}{A_{ions132}} = 108.3\ \%\ .$$

This result was close to the expected value of 98.1 %, thus demonstrating that the LEIS setup has the ability to test mass spectrometers with fast ions and that OpenTOF already delivers a satisfactory performance for high relative velocities. The current status of the LEIS equipment with a divergent beam might also partially prevent both LEIS and OpenTOF from showing their full performance potential. Schertenleib (2023) showed thanks to simulations that an angle between the incoming trajectory and the aperture's axis of symmetry of 2° or above leads to a significantly decreased performance of OpenTOF. A suggestion to solve this issue in a future version of the LEIS equipment is to place two parallel plates with a thin hole perpendicularly to the needed trajectory to act as a beam skimmer. Furthermore, a proposal to improve the LEIS setup is to use a grid in front of the conversion surface to enable a positive voltage to deviate the positive ions away from the beam. Consequently, the new equipment will be able to test mass spectrometers with fast neutrals only, i.e. without incoming ions. Furthermore, the ability to modulate the ratio between fast ions and fast neutrals will also be of interest, e.g. to investigate further the effect of ion concentration on thermal signal.

As of 2025, the Neutral and Ion Mass Spectrometer (NIM) is currently flying on board the JUpiter ICy moons Explorer (JUICE) mission to Jupiter. Furthermore NIM has a wider field of view than OpenTOF (Schertenleib, 2023) and LEIS will be used before the end of 2025 for this instrument. As demonstrated by this work, the current version of the LEIS equipment can already be useful as such for the oncoming NIM test and calibration campaign on a replica of the flight instrument in Bern.

4.2 Measurements with $C_{14}F_{24}$ at 7.65 km/s and Beyond

A second series of measurements was carried out, following the same procedure as in Section 4.1, but with FC5311 instead of xenon. FC5311 is a chemical compound containing $C_{14}F_{24}$, handy to use for mass spectrometer testing and calibration due to its wide mass range reaching 624 u. FC5311 is a liquid under normal room conditions. However, since the vacuum chamber with OpenTOF had a pressure between $2 \cdot 10^{-9}$ mbar and $9 \cdot 10^{-7}$ mbar, FC5311 could vaporise at room temperature without external heating to go through the inlet system and fill the vacuum chamber. The continuous filling of the chamber with the active cryopumps was constant enough to reach a stable pressure, often with a value of $(3.5 \pm 0.1) \cdot 10^{-7}$ mbar as targeted in Section **??**. The settings used for LEIS and OpenTOF are summarised in Table 4.2.

Parameter LEIS for $C_{14}F_{24}^{+}$ at 7.65 km/s	**Value**	**Parameter** OpenTOF for 16.6 km/s	**Value**
Cathode bias	119.3 V	Q-BP_Pulser	600 V
Extraction	170.0 V	Q-AccL	-1139 V
Ion box	190.3 V	Q-D_Pulser	-5000 V
Ion box exit grid	188.3 V	Drift	-5000 V
Electron collector grid	97.5 V	D-L	-2450 V
Electron collector	232 V	R-L0	-6000 V
Backplane and housing	GND = 0 V	VD-R_B	828 V
Electron emission	(5117 ± 30) μA	R-BP	1091 V
		MCP-F	-5000 V
		Anode	-2900 V
		Q-Gr	0.0 V
		$I_{Filament}$	(197 ± 4) μA

Table 4.2: Settings for the spectrum measurement of FC5311 ($C_{14}F_{24}$) at 7.65 km/s using OpenTOF and LEIS with its neutraliser.

A voltage interval of $[188.3, 190.3]$ V was used for measurement series 2. These energies yield a speed in the interval $[7.63, 7.67]$ km/s for $C_{14}F_{24}$. This interval was chosen because it contains 7.65 km/s, which is the speed of objects travelling around the Earth on a Low-Earth Orbit (LEO), such as the International Space Station, as explained in Section 1.1.1 (Chan and Zhou, 2018). Since the same potential is used to accelerate all ions in LEIS, singly-charged ions of lower masses or doubly-charged ions with the same mass have a higher speed than $C_{14}F_{24}^{+}$ when exiting LEIS. Thus, the velocities of the different ions and neutrals entering OpenTOF can differ to a large extent if the mass range is wide. Measurement series 2 recorded spectra over 10 μs and the result is displayed in Figure **??**. For this chosen voltage interval, the speed interval for a detected mass of 293 u was $[11.14, 11.20]$ km/s. Furthermore, CF_3^+ with a mass of 69 u was the highest peak and had a speed interval of $[22.95, 23.07]$ km/s. Finally, the lowest detected mass was 18, showing the presence of water due to the low quantity of remaining air in the vacuum chamber. H_2O^+ reached a high velocity whose magnitude was in the interval $[44.93, 45.17]$ km/s. A highest mass of 293 u was obtained, which does not show any limit of the instrument, but the simple need to set the acquisition software to record during e.g. 20 μs instead of only 10 μs for future measurement campaigns. A proven mass range of at least m/z 18 to 293 is already enough to conduct an interesting investigation of Io's volcanic atmosphere, since a range up to m/z 300 is needed according to Fausch et al. (2022b).

For a given mass, OpenTOF is designed to yield a longer time of flight for thermal particles than for fast particles. In space, this enables the instrument to tell apart thermal signals with a low relative velocity due to outgassing of the spacecraft from signals of particles with a high relative velocity belonging to the atmosphere of the investigated celestial body. In measurement series 2, the thermal signal was clearly visible even though the voltage set was optimised for fast particles. Moreover, for every peak due to fast particles, the corresponding thermal peak was shifted to a higher time of flight, thus to a higher mass, following the expected tendency: the higher the mass the higher the shift. This mass shift behaviour is consistent with xenon measurements from Section 4.1 and with simulations conducted by Schertenleib et al. (2024).

The signal pattern of measurement series 2 was regular over the full measured mass range and was even simpler to handle than for measurement series 1. A peak a is visible at the same measured time in the total signal and in the ion signal, but not in the thermal signal. Then, on the right, at a slightly higher time point, a peak b is visible in the total signal, and, on the same spot, it is also visible in the thermal signal, but not in the fast ion signal. Furthermore, this peak b is much taller in the thermal signal than in the total curve. Peak a is due to fast ions and fast neutrals. Thus, it is not visible on the thermal signal, but will be recorded by the other two. Peak b is due to thermal gas in the chamber, so it will not appear in the fast ion signal, but only in the other two. The reason why the thermal peaks are taller in the thermal measurement than in the total signal is the same as for xenon in Section 4.1: the thermal ion storage effect by the electron beam is decreased by the fast ion flux. The estimation of fast neutrals is simpler to handle than for the isotopes of xenon in measurement series 1, because in measurement series 2, every peak of fast particles was at least a few mass units away from the next peak. Thus, thermal peaks and fast particle peaks did not overlap, which means that the total signal was only made up of fast ions and fast neutrals, without any thermal component. Consequently, in zones in which a peak of fast particles was identified, the presence of fast neutrals could be estimated by subtracting the fast ion peak area from the total signal peak area.

The determination of the fast neutral counts with the subtraction of peak areas yielded low values close to the error margins. The high ion flux directly coming from LEIS hinders the electron ionisation process, as demonstrated by the lower thermal signal in both measurement series 1 and 2. Under the same conditions, with the same LEIS settings, namely the same fast neutral flux, a grid placed in front of the conversion surface before OpenTOF's aperture can solve the issue without any further major change. With the same neutral flux, but no impediment to electron ionisation, fast neutrals are likely to be more ionised and, thus, to be detected in clear peaks outside of error margins. Moreover, thanks to a skimmer, only lower angle ions will be generated, thus increasing the transmission as shown by simulations conducted by (Schertenleib, 2023).

Furthermore, for direct ions measured without OpenTOF's filament, the measurement was successful without fragmentation induced by high-velocity impact, as foreseen by Fausch et al. (2023). As a comparison, if the NIM mass spectrometer collects the same species with the same energy of 200 eV, the particles must go through NIM's antechamber to thermalise before entering the instrument and fragmentation of the parent species occurs during that phase (Föhn et al., 2021). To the author's best knowledge of the currently available space instruments, this measurement with OpenTOF is the first of its kind, achieving a mass spectrum detection with high velocities beyond 23 km/s without fragmentation.

m/z	**Formula**	**Speed [km/s]**
18	H_2O^+	[44.9, 45.2]
19	F^+	[43.7, 44.0]
28	N_2^+	[36.0, 36.2]
31	CF^+	[34.2, 34.4]
32	O_2^+	[33.7, 33.9]
50	CF_2^+	[27.0, 27.1]
69	CF_3^+	[22.9, 23.1]
93	$C_3F_3^+$	[19.8, 19.9]
100	$C_2F_4^+$	[19.1, 19.2]
112	$C_3F_4^+$	[18.0, 18.1]
119	$C_2F_5^+$	[17.5, 17.6]
131	$C_3F_5^+$	[16.6, 16.7]
143	$C_4F_5^+$	[15.9, 16.0]
162	$C_4F_6^+$	[15.0, 15.1]
169	$C_3F_7^+$	[14.6, 14.7]
181	$C_4F_7^+$	[14.1, 14.2]
193	$C_5F_7^+$	[13.7, 13.8]
205	$C_6F_7^+$	[13.3, 13.4]
219	$C_4F_9^+$	[12.8, 12.9]
231	$C_5F_9^+$	[12.5, 12.6]
243	$C_6F_9^+$	[12.2, 12.3]
255	$C_7F_9^+$	[11.9, 12.0]
267	$C_8F_9^+$	[11.6, 11.7]
286	$C_8F_{10}^+$	[11.2, 11.3]
293	$C_7F_{11}^+$	[11.1, 11.2]

Table 4.3: Detected masses from the spectrum of FC5311 for $C_{14}F_{24}$ at 7.65 km/s using OpenTOF and LEIS with its neutraliser. Formulae are taken from an article on time-of-flight measurements by Gasc and Hofer (2022).

Chapter 5

Conclusion

The author of this work maintained and improved the experimental setups of both devices, LEIS and the OpenTOF prototype, working in close collaboration with the mechanical and the electronics teams in the Unit for Space Research and Planetary Sciences at the University of Bern. He operated LEIS, thus generating both a fast ion beam and a fast neutral beam. Moreover, he chose a suitable tungsten filament with a diameter of 0.10 mm for the current and new version of LEIS, which has the purpose to serve for testing and calibration campaigns of future and current mass spectrometers. He characterised the fast ion beam, found proper operation settings, and created a conditioning and operation procedure for future needs of the team. Finally, the author managed to obtain a proof of concept for LEIS, showing its ability to be used on a real mass spectrometer prototype, such as OpenTOF. LEIS with its conversion surface now offers a practical and compact solution to generate a fast ion and neutral beam at speeds beyond 20 km/s, which are much higher than values of 5 km/s often found in classical systems using pressure Föhn et al. (2021). LEIS in its current version will be used in the autumn of 2025 for the ground calibration campaign of the Neutral and Ion Mass spectrometer, whose flight instrument is on board the JUICE mission, travelling to Jupiter as of August 2025.

Using LEIS with its neutraliser as a fast-beam generator, the author of this work also achieved a proof of concept for OpenTOF at high relative velocities even beyond the initial target of 20 km/s. Moreover, he experimentally determined optimised voltage sets to operate OpenTOF with different relative velocities above 5 km/s including 10 km/s and 20 km/s. Finally, he experimentally demonstrated the promising potentials of both instruments and their technical advantages for enhanced scientific benefits. Eventhough this work was centred around the operation of the OpenTOF prototype, it is also relevant to CubeSatTOF, since both mass spectrometers have the same novel Direct Open Source gas inlet.

This work reached numerous major milestones for the OpenTOF prototype. In thermal mode, a mass range of at least $[18, 643]$ was demonstrated, in agreement with the aimed range of $[1, 800]$ and previous measurements conducted by Iseli (2024). Fast ions up to 20 km/s with a mass of 84 were detected by OpenTOF, or 19.8 km/s for mass 93. Velocities even beyond 20 km/s for lower masses were achieved, with the highest speed of 45 km/s reached for mass 18. Masses even up to 136 for ions with speeds up to 19 km/s were detected, while fast ions beyond 11 km/s for masses up to 293 were clearly recorded by OpenTOF. Moreover, a proven ability of the instrument to separate fast particle signals of the investigated atmosphere from the thermal outgassing signal of the spacecraft was demonstrated. Finally, OpenTOF detected fast neutrals up to a mass of 132 at 17 km/s. This is a proof of concept for this novel Direct Open Source system. To the author's best knowledge of the currently available space instruments, this measurement with OpenTOF is the first of its kind, achieving a mass spectrum detection with high velocities of 17 km/s for neutral

gas and beyond 23 km/s for ions without any hypervelocity impact fragmentation. These results show that OpenTOF is a suitable instrument for new high relative velocity space missions with unmatched scientific benefits. OpenTOF can play a key role for the exploration of exospheres in the Solar System thanks to its design and its novel Direct Open Source.

Following the recommendations of this work, a grid for LEIS to suppress non-neutralsied ions is already in preparation as discussed above. Moreover, a skimmer would also decrease the beam divergence as previously explained and should also be considered in a future version of the LEIS setup. Finally, the delay-pulser has already been ordered and will be soon incorporated in the upgraded version of OpenTOF to enable the detection of masses above 530 at 20 km/s(Iseli, 2024; Schertenleib, 2023).

An even more advanced and practical testing setup could be achieved thanks to the following proposal, depicted in Figure5.1. A special Faraday cup a similar aperture as OpenTOF's could be mounted in the vacuum chamber next to OpenTOF, both instruments facing the same direction. In front of both instruments a moving table should be installed, which could be positioned from outside of the vacuum chamber thanks to an electric system. Therefore, new LEIS settings for given measurement needs with ions could be characterised without opening the vacuum chamber nor changing the setup, thus leading to more flexibility. In an ideal case, new grids could even be place in the vicinity of the Faraday cup to create a similar electric field environment to the conditions in front of OpenTOF. The new procedure to calibrate OpenTOF or any other mass spectrometer could be as follows.

I. Theoretically determine the needed LEIS settings, using results from this work.

II. Use the Faraday cup (FC) to characterise the ion beam and change the settings according to needed performance.

III. Move LEIS in front of OpenTOF and measure the beam with OpenTOF.

IV. Fine-tune the LEIS settings if required.

V. If the final LEIS settings do not match the initial values, move LEIS in front of the FC, and characterise the final ion beam.

This work delivered a proof of concept, showing that the instrument and its novel gas inlet fulfil their purposes at high relative velocities. Therefore, OpenTOF was proven to be a promising instrument for the near-future investigation of atmospheres in the Solar System.

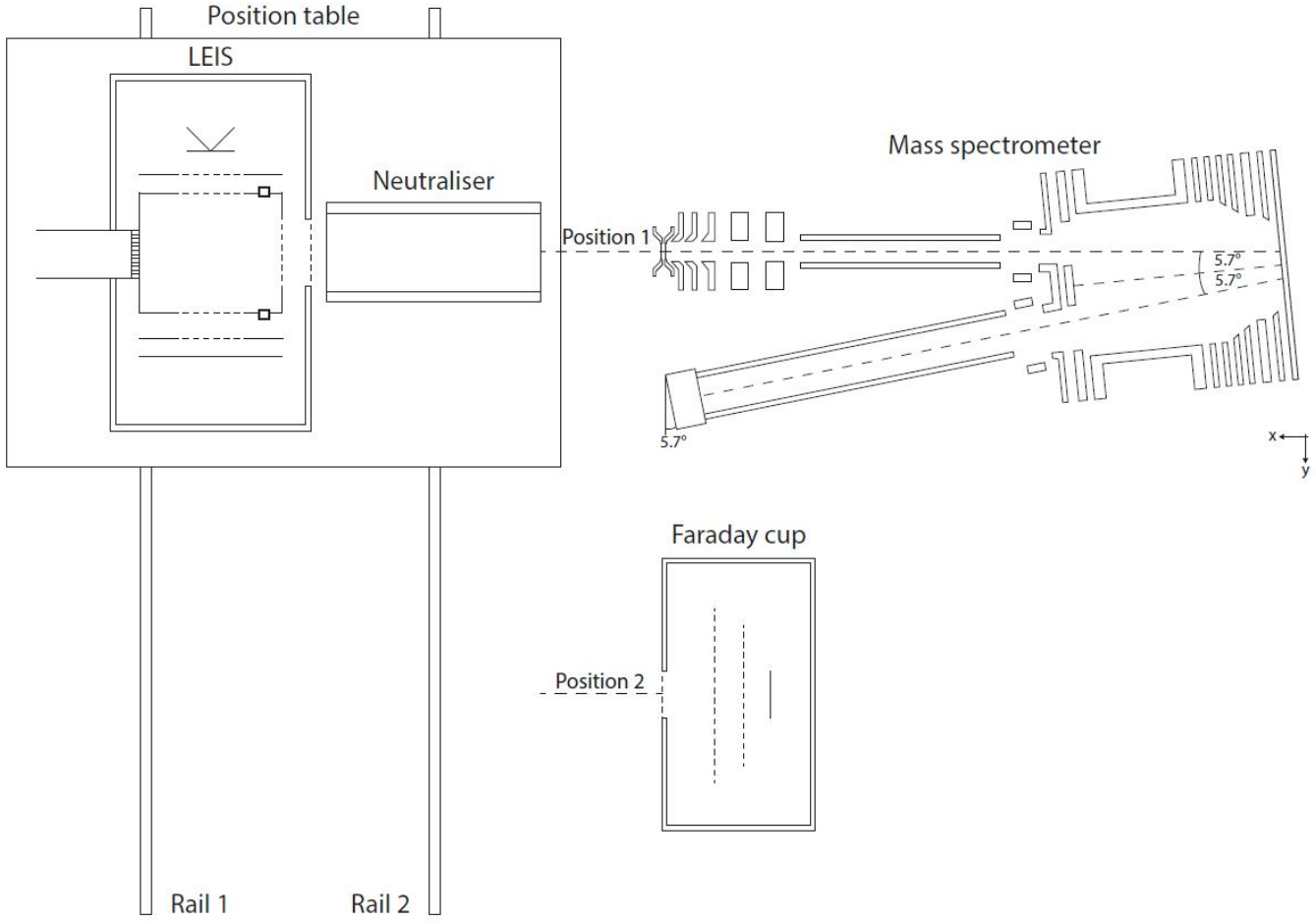

Figure 5.1: Schematic of a proposed future setup for efficient calibration and testing of mass spectrometers.

Acknowledgement

The author of this work would like to warmly thank his supervisors and laboratory coaches Rico Fausch, Peter Wurz, and Johann Far for providing him with the amazing opportunity to be part of the team and work on this stimulating project. The regular meetings and guidance were greatly appreciated. The learning experience, the positive work environment, the feeling of progress and purpose have been highly enriching. The author is also thankful to the assessment committee for reading his work and to every individual who also contributed to help, especially Alex Iseli, Samuel Wyler, Harald Mischler, Iljadin Manurung, Raphael Hänggi, and David Reis.

Kind messages are also sent to all family members, friends, professors, teachers, trainers, instructors who once helped, sometimes even without knowing. Denise, Johny, Neo, Richard, Mathis, David, Loli, Julio, Newton, Rainer, and Eliushkavril are not forgotten.

Finally, a strong feeling of gratitude and kindness is expressed towards those who are not explicitly named, but should know that they matter.

Thank you!

Appendix

Conditioning of the LEIS Electron Emission Wire

Sometimes, the vacuum chamber needs to be opened, *e.g.* when the instrument needs to be inspected or the setup modified. As a consequence, the Micro-Channel Plates (MCPs) of OpenTOF's detector and the electron emission wire of the LEIS need to be conditioned. Forgetting to condition the MCPs might lead to damage of the detector. In the case of the electron emission wire, conditioning is also important, because unstable emission was observed (*e.g.* an unexpected strong decrease). This subsection summarises the conditioning procedure for the LEIS wire, with which the author came up.

1. Leave the instrument in the vacuum chamber until the pressure is of the order of 10^{-8} mbar (*e.g.* below 10^{-7} mbar).

2. Set the LEIS for an ion speed of 10 km/s according to usual settings. The operator might decide to start the conditioning without gas. In the example displayed below Argon was let in only after 70 minutes.

3. Set the cathode voltage $U_{Cathode}$ to reach the needed electron emission current $I_{emission}$ (*i.e.* 100 μA for 10 km/s or 65 μA for 20 km/s). Increase $U_{Cathode}$ by about 0.1 - 0.2 V every second in order to prevent a too abrupt ramping-up. After about 2 to 5 minutes this voltage might be kept even if $I_{emission}$ is slightly decreasing.

4. Measure $I_{emission}$ with regard to time (without changing $U_{Cathode}$ to correct for the decrease of $I_{emission}$).

5. Regularly control the temperature T_{LEIS} of the LEIS. When T_{LEIS} reaches $[80, 100]°C$ ramp down the LEIS wire with about 0.5 V/s and let it cool down.

6. After 60 to 90 minutes correct $I_{emission}$ back to the wanted value thanks to an adaptation of $U_{Cathode}$. Regularly adapt the gas pressure in the vacuum chamber as needed (*e.g.* $3.5 \cdot 10^{-7}$ mbar). Start again at step 4.

7. When $T_{LEIS} > 80°C$, interrupt the running cycle, by ramping the LEIS wire down and let it cool down a few hours. When the wire was switched off, a temperature decrease of about $8°C$ per hour has been observed.

8. After 2 - 3 cathode running cycles or if the electron emission seems to stay within acceptable margins, the conditioning may be stopped. Examples of values reached for the change in $I_{emission}$ are about $\pm$ 0.25 μA/min for 10 km/s or $\pm$ 0.1 μA/min for 20 km/s. The instability does not always mean a decrease of $I_{emission}$, it might also lead to a slight increase throughout time.

9. After the first cathode running cycles with 10 km/s, the cathode should be running at least one cycle with the settings for an ion speed of 20 km/s following the same steps as described above.

The results of the conditioning test 1 for the LEIS electron emission wire are displayed in Figure 5.2. The orange points stand for the electron emission current $I_{emission}$ in μA, while the blue data represents the argon ion current I_{ion} in pA. For an ion speed of 10 km/s, according to previous tests, it was decided to aim for an $I_{emission}$ of about 100 μA. At the start, the pressure inside the gas chamber was 5.59 $(\pm 0.75) \cdot 10^{-8}$ $mbar$ for 96 minutes, before argon was let in, increasing the pressure to 3.51 $(\pm 0.03) \cdot 10^{-7}$ $mbar$. The cathode voltage $U_{cathode}$ was held at a constant value of 4.80 V for 70 minutes and then adapted from 5.07 V (5.37 W) to 5.23 V (6.14 W). The temperature was 23.3 $°C$ at the start and reached 64.9 $°C$ at the end, after 145 minutes.

$I_{emission}$ firstly started to increase under a constant cathode voltage, before dropping between 50 and 70 minutes with a high average rate of -5.2 $\mu A/min$ without argon in the vacuum chamber. Meanwhile, the average change in I_{ion} was about -0.3 pA/min. When $U_{cathode}$ was regularly adapted, $I_{emission} = 100.6$ (± 2.2) μA. When argon was in the chamber $I_{ion} = 214.05$ (± 4.03) pA. Thus, both current stayed stable to a relatively satisfactory level if $U_{cathode}$ was adapted every 3-10 minutes. The goal would have been to reach stable electron and ion currents without having to correct the cathode voltage throughout time.

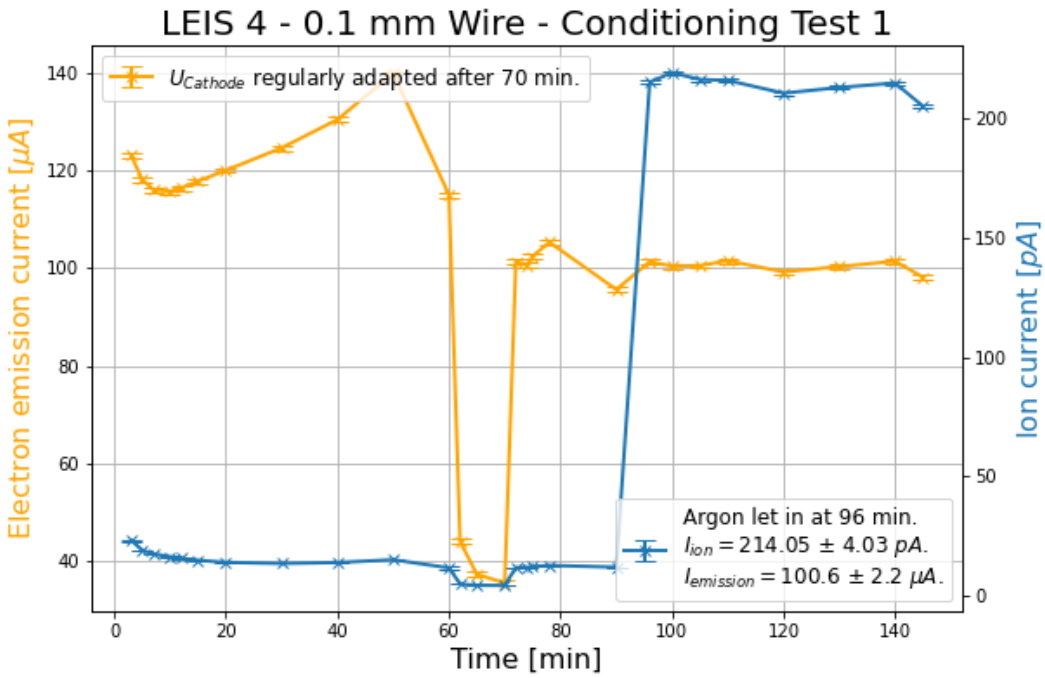

Figure 5.2: First test of the conditioning procedure for the LEIS electron emission wire after it had been air-exposed. The orange curve represents the electron emission current, while the blue curve is the resulting argon ion current. The voltage at the electron emission cathode was held constant for 70 minutes and, then, regularly adapted to keep the emission current around 100 μA. The aimed ion speed was 10 km/s.

Figure 5.3 shows test 2 of the conditioning procedure carried out on the day after test 1. As for

Figure 5.2, the orange data stands for the electron emission current $I_{emission}$ in μA, while the blue points represent the argon ion current I_{ion} in pA. However, in the case of test 2, the voltage at the electron emission cathode was adapted between two consecutive measurements since the beginning to keep the emission current around 100 μA. Furthermore, the same settings were used as for test 1 according to usual settings, in order to aim for an ion speed of 10 km/s. The temperature on the LEIS housing started at 22.4 $°C$ and gradually increased up to 60.4 $°C$ after 125 minutes.

It should be noted that the left and the right vertical axes do not have the same scale, nor the same range, to more conveniently fit both data sets on the same plot. Therefore, only a false impression of high fluctuation might be given to the reader, since the actual variation is only a few percent. Computing the mean and using the standard deviation as the uncertainty yields $I_{emission} = 101.5 \pm 1.4\ \mu A$ and $I_{ion} = 230.62 \pm 3.02\ pA$ for an average pressure with argon of $3.52\ (\pm\ 0.03) \cdot 10^{-7}\ mbar$. The rate at which the cathode voltage needed to be adapted was similar as for test 1. As it was the case for test 1, the relatively low standard deviations show a satisfactory degree of stability, even though the cathode voltage always had to be adapted. Finally the obtained values for the ion current are not exactly identical, but stay in the same range, as is displayed in Table 5.1.

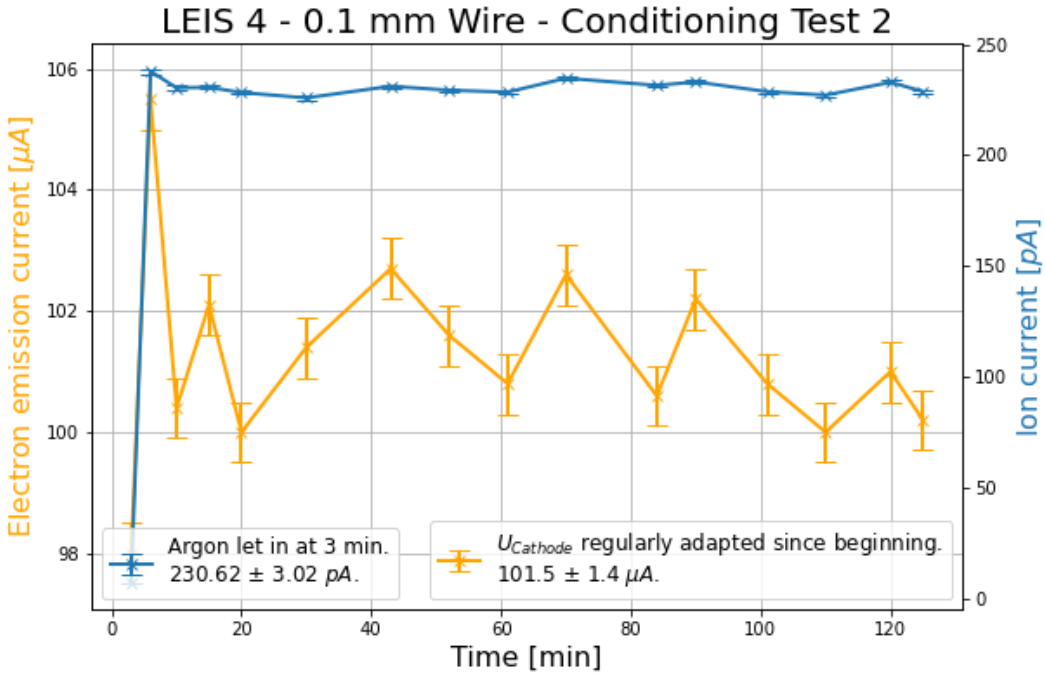

Figure 5.3: Test 2 of the conditioning procedure for the LEIS electron emission wire after it had been air-exposed (carried out the day after test 1). The orange curve represents the electron emission current, while the blue curve is the resulting argon ion current. Contrary to test 1, the voltage at the electron emission cathode was regularly adapted since the beginning to keep the emission current around 100 μA. The aimed ion speed was 10 km/s.

After test 2 the electron emission cathode was switched off about 3 hours to cool down. Then, test 3 was carried out, using the settings for an ion speed of about $20 km/s$, as usual. The temperature on the LEIS housing started at 35.7 $°C$ and reached 65.5 $°C$ after 124 minutes. Furthermore, the pressure with argon was kept around $3.52\ (\pm\ 0.02) \cdot 10^{-7}\ mbar$. The results of the conditioning test

3 are displayed in Figure 5.4.

As for test 2, the cathode voltage was adapted for every measurement, reaching 5.11 V (5.91 W). Thus, $I_{emission} = 64.7 \pm 1.7\ \mu A$ and $I_{ion} = 241.74 \pm 14.41\ pA$. Consequently, $I_{emission}$ was still satisfactory, but slightly less stable for test 2 with $10 km/s$ than during test 3 with $20 km/s$, as is summarised in Table 5.1.

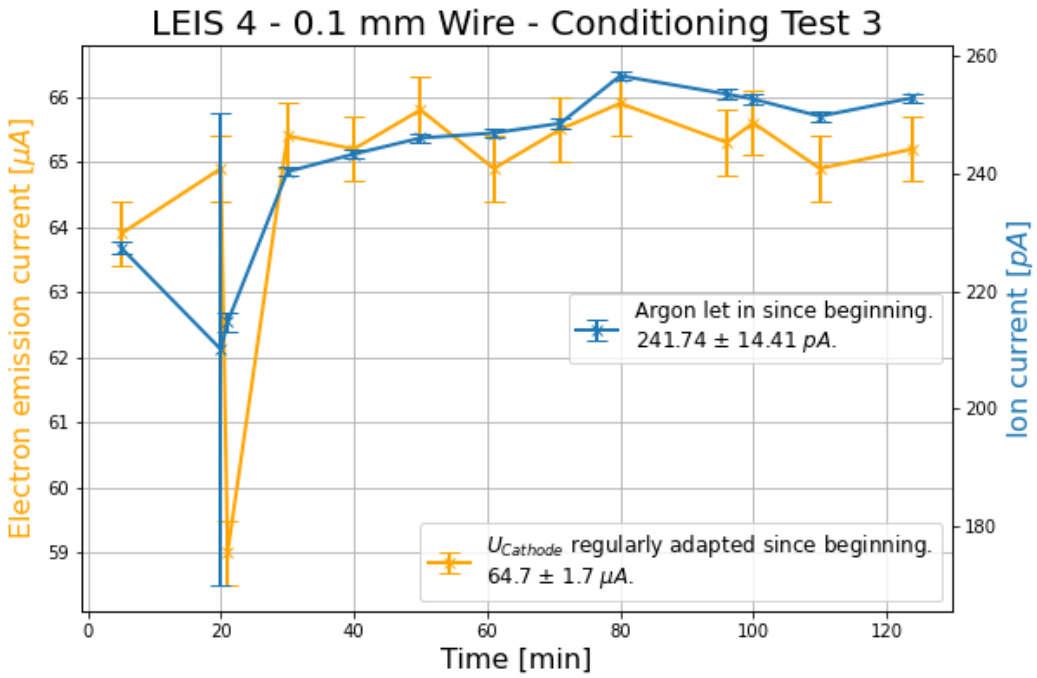

Figure 5.4: Test 3 of the conditioning procedure for the LEIS electron emission wire after it had been air-exposed (carried out after test 2 on the same day). The orange curve represents the electron emission current, while the blue curve is the resulting argon ion current. Contrary to test 1, the voltage at the electron emission cathode was regularly adapted since the beginning to keep the emission current around 65 μA. The aimed ion speed was 20 km/s.

Parameter	Test 1 with 10 km/s	Test 2 with 10 km/s	Test 3 with 20 km/s
P_{argon}	$3.51\ (\pm\ 0.03) \cdot 10^{-7}\ mbar$	$3.51\ (\pm\ 0.03) \cdot 10^{-7}\ mbar$	$3.52\ (\pm\ 0.03) \cdot 10^{-7}\ mbar$
$I_{emission}$	$100.6\ \pm 2.2\ \mu A$	$101.5 \pm 1.4\ \mu A$	$64.7 \pm 1.7\ \mu A$
I_{ion}	$214.05\ \pm 4.03\ pA$	$230.62 \pm 3.02\ pA$	$241.74 \pm 14.41\ pA$

Table 5.1: Comparaison of $I_{emission}$ and I_{ion} for the conditioning tests 1, 2, and 3 of the LEIS electron emission cathode (tungsten wire). Mean values are given with their standard deviations.

After the end of the conditioning test 3, a measurement of the energy spread was carried out for 20 km/s with a mean $I_{emission} = 63.0\ \mu A$ ($\sigma = 1.7$) and, then, for 10 km/s with a mean $I_{emission} = 93.0\ \mu A$ ($\sigma = 4.8$). The data analysis yielded a mean (μ) energy of 20.57 eV with a standard deviation (σ) of 1.59 eV for $10 km/s$ and $\mu = 83.20\ eV$ with $\sigma = 1.62\ eV$ for 20 km/s.

For an assumed Gaussian distribution of the data, there is a probability of about 95.4% for the measured value to be in the interval $[\mu - 2 \cdot \sigma, \mu + 2 \cdot \sigma]$. Furthermore, the computed energies can be converted to speeds for the argon ion. As a consequence, these results might be interpreted as follows. More than 95% of argon ions have a speed in the interval $[9.2, 10.7]$ km/s in the first case and in the interval $[19.7, 20.4]$ km/s in the other.

Bibliography

Ken Chan and Weiping Zhou. **Statistical Pairwise Collision Probability of the International Space Station with Debris**. 01 2018. doi: 10.2514/6.2018-2230.

J.S. Coursey, D.J. Schwab, J.J. Tsai, and R.A Dragoset. **Atomic Weights and Isotopic Compositions (version 4.1)**. https://physics.nist.gov/cgi-bin/Compositions/stand_alone.pl?ele=129&all=all&isotype=all, 2015. National Institute of Standards and Technology. Last consulted on 01/08/2025.

Edmond de Hoffmann and Vincent Stroobant. ***Mass Spectrometry: Principles and Applications***. John Wiley and Sons Ltd, Chichester, third edition, 2007.

P. Desai, T. Chu, H. James, and C.-Y Ho. **Electrical Resistivity of Selected Elements**. *Journal of Physical and Chemical Reference Data - J PHYS CHEM REF DATA*, 13, 10 1984. doi: 10.1063/1.555723.

Rico Fausch, Peter Wurz, Marek Tulej, and Urs Rohner. **CubeSatTOF: Planetary Atmospheres Analyzed with a 1U High-Performance Time-Of-Flight Mass Spectrometer**. 07 2020.

Rico Fausch, Gregor Moeller, Markus Rothacher, Nicolas Martinod, Tristan Trebaol, Alfonso Villegas, Jean-Paul Kneib, François Corthay, Marcel Joss, Tieche François, Marek Tulej, and Peter Wurz. **CHESS: Measuring the Dynamics of Composition and Density of Earth's Upper Atmosphere with CubeSats**. *IEEE Aerospace Conference Proceedings*, 43, 03 2022.

Rico Fausch, Peter Wurz, Björn Cotting, Urs Rohner, and Marek Tulej. **Direct Measurement of Neutral Gas during Hypervelocity Planetary Flybys**. *IEEE Aerospace Conference Proceedings*, 43, 03 2022a.

Rico Fausch, Janis Schertenleib, and Peter Wurz. **Reliably Analyzing the Chemical Composition of Plumes during Flybys at Velocities Exceeding 5 km/s**. pages 1–8, 03 2023. doi: 10.1109/AERO55745.2023.10115795.

Rico Fausch, Martina Föhn, Lukas Hofer, Stefan Meyer, Peter Wahlström, Samuel Wyler, and Peter Wurz. **Power-Efficient Electron Emitters for Electron Ionization in Spaceborne Mass Spectrometers**. pages 1–19, 03 2024. doi: 10.1109/AERO58975.2024.10521278.

Rico G. Fausch, Janis A. Schertenleib, and Peter Wurz. **Advances in Mass Spectrometers for Flyby Space Missions for the Analysis of Biosignatures and Other Complex Molecules**. *Universe*, 8(8):416, August 2022b. doi: 10.3390/universe8080416.

E. Flamini, A. Adriani, J. W. Armstrong, F. Capaccioni, G. Filacchione, L. Iess, G. Mitri, and S. Viviano. **A unique mission: Cassini-Huygens, the Orbiter, the descent Probe and**

the cruise science. *Nuovo Cimento Rivista Serie*, 42(5):197–259, June 2019. doi: 10.1393/ncr/i2019-10159-y.

Martina Föhn, Andre Galli, Audrey Vorburger, Marek Tulej, Davide Lasi, Andreas Riedo, Rico Fausch, Michael Althaus, Stefan Brüngger, Philipp Fahrer, Michael Gerber, Matthias Lüthi, Hans Munz, Severin Oeschger, Daniele Piazza, and Peter Wurz. **Description of the Mass Spectrometer for the Jupiter Icy Moons Explorer Mission**. pages 1–14, 03 2021. doi: 10.1109/AERO50100.2021.9438344.

Sébastien Gasc and Lukas Hofer. **Novel Time-of-Flight Residual Gas Analyzer (TOF-RGA) for in situ Real-time Process Monitoring**. *CHIMIA*, 76:52, 02 2022. doi: 10.2533/chimia.2022.52.

Martin C. E. Huber, Anuschka Pauluhn, J. Culhane, Gethyn Timothy, Klaus Wilhelm, and Alex Zehnder. ***Observing Photons in Space: A Guide to Experimental Space Astronomy***. 01 2013. ISBN 978-1-4614-7803-4. doi: 10.1007/978-1-4614-7804-1.

Inficon. ***Transpector CPM Calibration Reference***, 2005. Technical Note on FC5311.

Alex Iseli. **Calibration of Time-of-Flight Mass Spectrometers for High-Velocity Fly-bys and Ground-Based Applications**, 2024. University of Bern.

Davide Lasi, Stefan Meyer, Daniele Piazza, Mathias Lüthi, Andreas Nentwig, Mario Gruber, Stefan Brüngger, Michael Gerber, Saverio Braccini, Marek Tulej, Martina Föhn, and Peter Wurz. **Decisions and Trade-Offs in the Design of a Mass Spectrometer for Jupiter's Icy Moons**. In *2020 IEEE Aerospace Conference*, pages 1–20, 2020. doi: 10.1109/AERO47225.2020.9172784.

Shannon MacKenzie, Marc Neveu, Alfonso Davila, Jonathan Lunine, Morgan Cable, Charity Phillips-Lander, Jennifer Eigenbrode, J. Waite, Kate Craft, Jason Hofgartner, Chris McKay, Christopher Glein, Dana Burton, Samuel Kounaves, Richard Mathies, Steven Vance, Michael Malaska, Robert Gold, Christopher German, and Jennifer Heldmann. **Science Objectives for Flagship-Class Mission Concepts for the Search for Evidence of Life at Enceladus**. *Astrobiology*, 22, 03 2022. doi: 10.1089/ast.2020.2425.

Ryan Park, R. Jacobson, L. Casajus, F. Nimmo, A. Ermakov, J. Keane, W. McKinnon, David Stevenson, R. Akiba, B. Idini, D. Buccino, A. Magnanini, Marzia Parisi, Paolo Tortora, Marco Zannoni, A. Mura, Daniele Durante, L. Iess, J. Connerney, and Scott Bolton. **Io's tidal response precludes a shallow magma ocean**. *Nature*, 638:69–73, 12 2024. doi: 10.1038/s41586-024-08442-5.

Julie Reveillaud, Emily Reddington, Jill Mcdermott, Christopher Algar, Julie Meyer, Sean Sylva, Jeffrey Seewald, Christopher German, and Julie Huber. **Subseafloor microbial communities in hydrogen-rich vent fluids from hydrothermal systems along the Mid-Cayman Rise**. *Environmental Microbiology*, 18:n/a–n/a, 12 2016. doi: 10.1111/1462-2920.13173.

Martin Rubin, Kathrin Altwegg, Annette Jäckel, and Hans Balsiger. **Development of a low energy ion source for ROSINA ion mode calibration**. *Review of Scientific Instruments*, 77:103302–103302, 10 2006. doi: 10.1063/1.2358708.

Janis Schertenleib. **Development and Optimisation of Time-of-Flight Mass Spectrometers for Neutral Gas Measurements at High Relative Speeds**, 2023. University of Bern.

Janis Schertenleib, Rico G. Fausch, and Peter Wurz. **Ion-Optical Design of a Mass Spectrometer for Analyzing Complex Molecules during Fast Flybys**. In *2024 IEEE Aerospace Conference*, pages 1–7, 2024. doi: 10.1109/AERO58975.2024.10521245.

Scott Sheppard, David Tholen, Mike Alexandersen, and Chadwick Trujillo. **New Jupiter and Saturn Satellites Reveal New Moon Dynamical Families**. *Research Notes of the AAS*, 7: 100, 05 2023. doi: 10.3847/2515-5172/acd766.

Justyna M. Sokół, Jianliang Lin, Stephen A. Fuselier, Travis Eliason, John E. Gomez, Benjamin Rodriguez, John N. Pham, Clark Schiferl, Christopher Rincon, Cedric Bernier, Caden Andersson, Felicia Mendoza, Jonathan Gasser, Peter Wurz, André Galli, Eric Hertzberg, and Nathan A. Schwadron. **Diamond-like carbon conversion surfaces for space applications**. *Journal of Applied Physics*, 135(18):185301, May 2024. doi: 10.1063/5.0203686.

Eite Tiesinga, Peter J. Mohr, David B. Newell, and Barry N. Taylor. **2022 Committee on Data for Science and Technology (CODATA) Recommended Values of the Fundamental Physical Constants (Version 9.0)**. https://www.physics.nist.gov/cuu/Constants/index.html, 2022. Database developed by J. Baker, M. Douma, and S. Kotochigova at the National Institute of Standards and Technology. Last consulted on 01/08/2025.

Peter Wurz, Dominic Abplanalp, Marek Tulej, and Helmut Lammer. **A neutral gas mass spectrometer for the investigation of lunar volatiles**. *Planetary and Space Science*, 00:00, 05 2012. doi: 10.1016/j.pss.2012.05.016.